

10-10-2022

Direct Material Property Determination: One-Dimensional Formulation Utilising Full-Field Deformation Measurements

Sreehair Rajan-Kattil

Michael A. Sutton

University of South Carolina - Columbia, sutton@cec.sc.edu

Subramani Sockalingam

Frank Thomas

Tusit Weerasooriya

See next page for additional authors

Follow this and additional works at: https://scholarcommons.sc.edu/phar_facpub



Part of the [Pharmacy and Pharmaceutical Sciences Commons](#)

Publication Info

Published in *Strain*, 2022.


© 2022 The Authors. *Strain* published by John Wiley & Sons Ltd. This is an open access article under the terms of the Creative Commons Attribution-NonCommercial-NoDerivs License, which permits use and distribution in any medium, provided the original work is properly cited, the use is non-commercial and no modifications or adaptations are made.

This Article is brought to you by the Pharmacy, College of at Scholar Commons. It has been accepted for inclusion in Faculty Publications by an authorized administrator of Scholar Commons. For more information, please contact digres@mailbox.sc.edu.

Author(s)

Sreehair Rajan-Kattil, Michael A. Sutton, Subramani Sockalingam, Frank Thomas, Tusit Weerasooriya, and Stephen Alexander

Direct material property determination: One-dimensional formulation utilising full-field deformation measurements

Sreehari Rajan-Kattil¹ | Michael A. Sutton¹  | Subramani Sockalingam¹ | Frank Thomas¹ | Tusit Weerasooriya² | Stephen Alexander³

¹Department of Mechanical Engineering, University of South Carolina, Columbia, South Carolina, USA

²US Army Research Laboratory, Aberdeen, Maryland, USA

³SURVICE Engineering Company, Belcamp, Maryland, USA

Correspondence

Michael A. Sutton, Department of Mechanical Engineering, University of South Carolina, Columbia, SC 29208, USA.

Email: sutton@sc.edu

Funding information

Army Research Laboratory, Grant/Award Number: W911NF-20-2-0231

Abstract

A direct approach is described to determine the elastic modulus distribution in a nominally heterogeneous material subject to tensile/compression loading and primarily experiencing deformations in the axial direction. The formulation is developed for uniaxial applications using basic theoretical constructs, resulting in a computational framework that has a matrix form $[A] \{E\} = \{R\}$, where the $[A]$ matrix components are known functions of measured axial strains and axial positions, $\{R\}$ components are known functions of axial body forces, applied loads and reactions and $\{E\}$ components are the unknown elastic moduli at discrete locations along the length of the specimen. For a series of one-dimensional (1D) material property identification procedure with known axial strains at discrete locations and various levels of random noise, results are presented to demonstrate the accuracy and noise sensitivity of the methodology. Finally, experimental measurements for a heterogeneous bone specimen are compared to our 1D model predictions, demonstrating that the predictions are in very good agreement with independent estimates at each load level of interest along the length of the bone specimen.

KEYWORDS

1D material property identification, direct material property determination, experimental application, finite element model, heterogeneous materials, one-dimensional formulation

1 | INTRODUCTION

Developments in the previous millennium that resulted in the broad distribution of robust, accurate digital image correlation methods to obtain full-field deformation measurements^[1–6] have led to increasing interest in novel ways to utilise the data that were not accessible previously. In particular, the methodology has been investigated for material property identification, especially in heterogeneous and anisotropic material systems that are more difficult to characterise.

Prior to the development of DIC methods, a common approach was to bond strain gages to specimens and use the discrete strain measurements with global stress estimates to estimate material properties. Since strain gages are not appropriate for soft materials, a few years before the ascent of DIC methods for full-field measurements, researchers in the medical imaging field began studying approaches to determine material properties in soft tissues using ultrasound

This is an open access article under the terms of the [Creative Commons Attribution-NonCommercial-NoDerivs](https://creativecommons.org/licenses/by-nc-nd/4.0/) License, which permits use and distribution in any medium, provided the original work is properly cited, the use is non-commercial and no modifications or adaptations are made.

© 2022 The Authors. *Strain* published by John Wiley & Sons Ltd.

images. In 1994, Raghaven and Yagle^[7] used ultrasound images to determine through-thickness strains at various locations in a tissue sample when subjected to mechanical loads. By rearranging a set of finite difference equations for equilibrium in an elastic material, the authors indicated that they were able to obtain the elastic properties. In 1996, Kallel published one of the first 'correlation-based' articles^[8] for material property determination, describing how to estimate the elastic properties of biological tissues. In his study, the author combined (a) property updating in an elastic finite element model for nominally 'known' loads with (b) ultrasound-based image correlation motion measurements on the tissue. During the analysis process, the authors noted that forces should be 'measured' at the boundary nodes; issues with boundary conditions were also noted in Raghaven and Yagle.^[7] Since the use of micro-scale load cells was impractical for the soft tissue specimens, the authors suggested using a known material between the specimen and the loading surface. By applying load to the known material, while simultaneously obtaining full-field strains on the material during loading, the strain data could be used to determine the surface stresses (and hence forces) on the specimen. Once all required conditions were known, the authors minimised the difference between the measured and predicted displacements by iteratively updating the material properties to obtain optimal property estimates. Finally, noting concerns regarding ill-conditioning of the matrices, the authors used Tikhonov regularisation as a compromise between fidelity to the observed data and a priori information regarding the range of elastic properties in the tissue, with convergence in the regularised solution occurring within a few iterations for an echo-cardiogram image set.

For micro-scale measurements required to characterise materials in MEMS devices, in 2009, Kamat^[9] reviewed the state of the art, remarking that extraction of micro-scale tensile specimens with average stress and average strain data as the basis for material characterisation were oftentimes used, with the interferometric strain/displacement gage method of Sharpe^[10] providing a way to obtain average strain data in specific regions, even when applying a broad range of temperatures. Near the turn of the millennium, Chasiotis and Knauss^[11] demonstrated the use of atomic force microscopy (AFM) with 2D-DIC for regions of the order of 100 μm in size to obtain full-field deformation measurements that could be used to obtain highly localised material property estimates. When using full-field measurements with computational models, as noted by Kallel,^[8] ill-posed matrices may complicate the inversion process necessary to determine an optimal set of material properties. One approach that was described for fracture problems by Réthoré et al.^[12] is to require least noise sensitivity for the parameter of interest during the optimisation process.

In the mid-2000s, two review articles focusing on the use of full-field methods for material property identification were published.^[13,14] In particular, Hild and Roux^[13] stated that DIC methods were needed to obtain elastic properties in heterogeneous materials where single measurements are not sufficient to fully characterise the material property distribution. In their review, the authors noted that minimisation of the difference between measurements and theoretical predictions using the material parameters provides an iterative methodology for optimal property identification. In a more detailed follow-on review,^[14] Avril et al. noted that a direct finite element approach would result in a computational form $K(\theta)U = F$ where K is the stiffness matrix that is a function of the material parameters, θ , U is the nodal displacement vector and F is the force vector. A variety of methods were discussed that could be used to determine material properties, including finite element method updating, virtual fields method, equilibrium gap and related approaches that minimise a specific function to determine an optimal set of material parameters. In addition to these methodologies, the authors also observed that $K(\theta)$ oftentimes can be written in a form $\sum K_i \theta_i$ when the matrix is a linear function of the material parameter set.

A global DIC-based method, commonly known as integrated DIC (IDIC), has been developed and extensively applied for parameter identification procedure in recent years. For example, Neggers et al.^[15] showed that time-resolved IDIC can be applied for material property identification by combining finite element method and DIC measurements at all time increments. Bertin et al.^[16] applied the IDIC method for material property identification of an elasto-plastic material using biaxial experimental data. In another study, Bertin et al.^[17] applied the IDIC method using 3D surface displacement data, load history and confocal microscopy to measure the height profile at the micro-scale to estimate crystal plasticity parameters.^[17] These approaches are based on finite element model updating (FEMU) method for material property identification.^[18,19] For example, Hartmann and Gilbert^[20] applied FEMU along with full-field strain measurement using DIC for material property identification of rubber-like material. In another study, Chelleni et al.^[21] applied FEMU for damage detection in a steel concrete composite frame. For a material system with large number of unknown properties, the direct method ($K(\theta)U = F$ ^[14]) has been shown to be computationally less expensive than the iterative method (FEMU).

In the enclosed work, the authors use concepts described in literature^[14] to develop a direct solution method for the distribution of Young's modulus in a heterogeneous, nominally one-dimensional (1D) component, subjected to either tension or compression loading. The method does not require iterative updating, thereby reducing computational

overhead, especially when there are large numbers of parameters to be determined. Compared to the IDIC method, the direct approach shown in this work has no restriction on the type of measurement method used to obtain the strain data while also allowing some flexibility in the element size based on the strain resolution and noise in the measured data. Though the method is readily applied to dynamic situations where specimen accelerations are measured, the focus in this study is on development and validation of the quasi-static formulation. To obtain the basic equations, a direct approach based on a Galerkin finite element formulation is employed. When given either measured displacements or strains, along with a measured force at either end, the resulting linear set of equations is then solved to determine the unknown material property distribution along the entire length of the specimen. In Section 2, the basic theory used in the method is described, and the 1D material property identification equations are presented. Section 3 described the numerical method used to obtain the axial distribution of Young's modulus and presents 1D material property identification procedure results using synthetic displacement and strain data with Gaussian random noise. Section 4 presents results when applying the methodology to a nominally 1D bone specimen that is subjected to uniaxial compression loading. Section 5 provides a discussion of results.

2 | THEORETICAL FORMULATION

A schematic of the 1D problem considered in this work, the coordinate system, the applied axial loading and specimen dimensions are shown in Figure 1.

The equation of equilibrium for a 1D bar can be written as

$$\frac{d\sigma}{dx} + f(x) = 0 \tag{1}$$

where $f(x)$ is the body force per unit volume, σ is the axial stress and x is distance along the bar axis.

The force boundary condition can be written in terms of the axial stress as

$$\sigma(x=L) = \frac{P}{A(x=L)} \tag{2}$$

where $A(x)$ is the cross-sectional area and P is the equilibrated axial static load.

Assuming a linear elastic constitutive relationship, Equations (1) and (2) can be written in terms of Young's modulus, E , and axial strain, ϵ , as follows.

$$\frac{d(E(x)\epsilon(x))}{dx} + f(x) = 0 : E(x=L) = \frac{P}{\epsilon(x=L)A(x=L)} \tag{3}$$

where, $\epsilon(x) = \frac{du}{dx}$, u is the axial displacement and $P/A(x) = \sigma(x)$. A solution for Equation (3), with $E(x)$ as the unknown variable, is sought using the finite element method.

The weak form for Equation (3) can be written as

$$\int_0^L \left[\frac{d(E(x)\epsilon(x))}{dx} + f(x) \right] w(x)A(x)dx = 0 \tag{4}$$

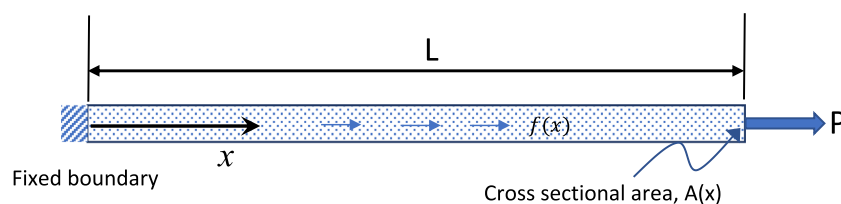


FIGURE 1 One-dimensional bar undergoing loading due to point load (P) and body force ($f(x)$)

where $w(x)$ is a weighting function. Using integration by parts, this can be written as

$$w(x)E(x)\varepsilon(x)A(x)\Big|_{x=0}^{x=L} - \int_0^L \frac{dw(x)}{dx} E(x)\varepsilon(x)A(x)dx + \int_0^L f(x) w(x)A(x)dx = 0 \quad (5)$$

Comparison of Equation (4) to the virtual field's method shows similar forms, with the weighting function related to kinematically admissible virtual field displacements. In the enclosed study, the weighting functions are assumed to be piecewise continuous functions across all elements.

Reordering the terms, Equation (5) can be written as

$$\int_0^L \frac{dw(x)}{dx} E(x)\varepsilon(x)A(x)dx = w(x) E(x)\varepsilon(x)A(x)\Big|_{x=0}^{x=L} + \int_0^L f(x) w(x)A(x)dx \quad (6)$$

2.1 | Finite element formulation

Figure 2a shows the discretisation of the domain into n elements.

The element-level equations for the i th element are shown in terms of natural coordinates and local node numbers as follows. Assuming a linear shape function for the approximate solution in each element, Young's modulus distribution in each element can be expressed as

$$E(\xi^{e_i}) = E_i(1 - \xi^{e_i}) + E_{i+1}\xi^{e_i} \quad (7)$$

where e_i represents element number, ξ^{e_i} is the local natural coordinate of the element as shown in Figure 2b ($\xi^{e_i} = 0$ at Node 1 and $\xi^{e_i} = 1$ at Node 2 in element i) and E_i and E_{i+1} are the nodal values of Young's modulus at nodes i and $i + 1$, respectively. The shape functions are also shown in Figure 2b, with $N_1 = (1 - \xi^{e_i})$ and $N_2 = \xi^{e_i}$.

The global to natural coordinate system transformation is written as

$$x = x_i(1 - \xi^{e_i}) + x_{i+1}\xi^{e_i} \quad (8)$$

where x_i and x_{i+1} are coordinates of nodes 1 and 2 in element i in the global coordinate system.

Applying the Galerkin method, there are two weighting function for a two-noded element.

$$\begin{aligned} w_1 &= N_1^{e_i} = (1 - \xi^{e_i}) \\ w_2 &= N_2^{e_i} = \xi^{e_i} \end{aligned} \quad (9)$$

Element-level equations are obtained by substituting the shape functions into the weak form of the equilibrium equations (Equation 6) and using the transformation equation given in Equation (8).*

$$\int_0^1 \left[J^{e_i-1} \frac{dN_1^{e_i}}{d\xi^{e_i}} (E_i N_1^{e_i} + E_{i+1} N_2^{e_i}) \right] \varepsilon(\xi^{e_i}) A(\xi^{e_i}) J^{e_i} d\xi^{e_i} = (N_1^{e_i} E(\xi^{e_i}) \varepsilon(\xi^{e_i}) A(\xi^{e_i})) \Big|_{\xi^{e_i}=0}^{\xi^{e_i}=1} + \int_0^1 f(\xi^{e_i}) N_1^{e_i} A(\xi^{e_i}) J^{e_i} d\xi^{e_i} \quad (10)$$

$$\int_0^1 \left[J^{e_i-1} \frac{dN_2^{e_i}}{d\xi^{e_i}} (E_i N_1^{e_i} + E_{i+1} N_2^{e_i}) \right] \varepsilon(\xi^{e_i}) A(\xi^{e_i}) J^{e_i} d\xi^{e_i} = (N_2^{e_i} E(\xi^{e_i}) \varepsilon(\xi^{e_i}) A(\xi^{e_i})) \Big|_{\xi^{e_i}=0}^{\xi^{e_i}=1} + \int_0^1 f(\xi^{e_i}) N_2^{e_i} A(\xi^{e_i}) J^{e_i} d\xi^{e_i} \quad (11)$$

*Repeated indices are not summed unless otherwise specified.

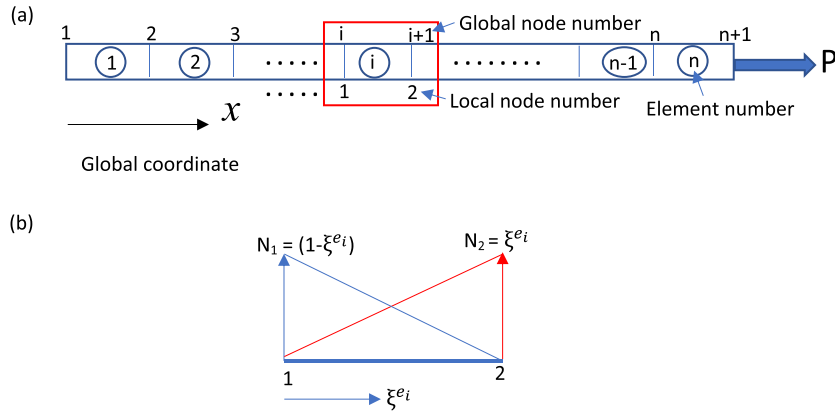


FIGURE 2 (a) Finite element discretisation of the one-dimensional bar loaded in tension, (b) linear shape functions for i th element

where the global derivatives are converted to derivatives with respect to the natural coordinates using the Jacobian, J^{ei} ; for the i^{th} element.

$$\frac{d}{dx} = J^{ei-1} \frac{d}{d\xi^{ei}} \tag{12}$$

The term $E(\xi^{ei})\epsilon(\xi^{ei})$ on the right-hand side of Equations (10) and (11) can be written as

$$E(\xi^{ei})\epsilon(\xi^{ei}) = \sigma(\xi^{ei}) \tag{13}$$

where σ is the Cauchy stress in the axial direction so that

$$\int_0^1 \left[J^{ei-1} \frac{dN_1^{ei}}{d\xi^{ei}} (E_i N_1^{ei} + E_{i+1} N_2^{ei}) \right] \epsilon(\xi^{ei}) A(\xi^{ei}) J^{ei} d\xi^{ei} = (N_1^{ei} \sigma(\xi^{ei}) A(\xi^{ei})) \Big|_{\xi^{ei}=0}^{\xi^{ei}=1} + \int_0^1 f(\xi^{ei}) N_1^{ei} A(\xi^{ei}) J^{ei} d\xi^{ei} \tag{14}$$

$$\int_0^1 \left[J^{ei-1} \frac{dN_2^{ei}}{d\xi^{ei}} (E_i N_1^{ei} + E_{i+1} N_2^{ei}) \right] \epsilon(\xi^{ei}) A(\xi^{ei}) J^{ei} d\xi^{ei} = (N_2^{ei} \sigma(\xi^{ei}) A(\xi^{ei})) \Big|_{\xi^{ei}=0}^{\xi^{ei}=1} + \int_0^1 f(\xi^{ei}) N_2^{ei} A(\xi^{ei}) J^{ei} d\xi^{ei} \tag{15}$$

The shape functions at local Nodes 1 and 2 are given by

$$N_1^{ei} \Big|_{\xi^{ei}=1} : N_2^{ei} \Big|_{\xi^{ei}=0} = 0 \tag{16}$$

$$N_1^{ei} \Big|_{\xi^{ei}=0} : N_2^{ei} \Big|_{\xi^{ei}=1} = 1 \tag{17}$$

with the shape function derivatives as

$$\frac{dN_1^{ei}}{d\xi^{ei}} = -1 : \frac{dN_2^{ei}}{d\xi^{ei}} = 1 \tag{18}$$

Substituting Equations (16)–(18) into Equations (14) and (15) gives

$$E_i \int_0^1 N_1^{ei} \epsilon(\xi^{ei}) A(\xi^{ei}) d\xi^{ei} + E_{i+1} \int_0^1 N_2^{ei} \epsilon(\xi^{ei}) A(\xi^{ei}) d\xi^{ei} = F_1^{ei} - \int_0^1 f(\xi^{ei}) N_1^{ei} A(\xi^{ei}) J^{ei} d\xi^{ei} \tag{19}$$

$$E_i \int_0^1 N_1^{ei} \epsilon(\xi^{ei}) A(\xi^{ei}) d\xi^{ei} + E_{i+1} \int_0^1 N_2^{ei} \epsilon(\xi^{ei}) A(\xi^{ei}) dx^{ei} = F_2^{ei} + \int_0^1 f(\xi^{ei}) N_2^{ei} J^{ei} A(\xi^{ei}) d\xi^{ei} \tag{20}$$

where $F_1^{e_i}$ and $F_2^{e_i}$ are the internal forces at local Nodes 1 and 2 in element i , respectively, ($F_1^{e_i} = \sigma(\xi^{e_i} = 0)A(\xi^{e_i} = 0)$ and $F_2^{e_i} = \sigma(\xi^{e_i} = 1)A(\xi^{e_i} = 1)$).

Equations (19) and (20) give the conditions for stress equilibrium as

$$F_1^{e_i} - \int_0^1 f(\xi^{e_i}) N_1^{e_i} A(\xi^{e_i}) J^{e_i} d\xi^{e_i} = F_2^{e_i} + \int_0^1 f(\xi^{e_i}) N_2^{e_i} A(\xi^{e_i}) J^{e_i} d\xi^{e_i} \quad (21)$$

Since $N_1^{e_i} + N_2^{e_i} = 1$, Equation (21) can be written as

$$F_1^{e_i} = F_2^{e_i} + \int_0^1 f(\xi^{e_i}) J^{e_i} A(\xi^{e_i}) d\xi^{e_i} \quad (22)$$

In global coordinates, Equation (22) can be written as

$$F_i = F_{i+1} + \int_{x_i}^{x_{i+1}} f(x) A(x) dx \quad : i = 1, 2, \dots, n+1 \quad (23)$$

where x_i and x_{i+1} are global coordinates of nodes i and $i+1$, respectively.

For the boundary element (where traction is specified), $F_{n+1} = P$. Thus, if the distributed body force and boundary traction can be measured accurately, stresses at all nodes can be determined using Equation (23).

To obtain direct equations for the unknown Young's moduli in each element, the element level equations can be assembled to give

$$\begin{bmatrix} A_{11} & \cdots & 0 \\ \vdots & \ddots & \vdots \\ 0 & \cdots & A_{nn} \end{bmatrix} \begin{bmatrix} E_1 \\ \vdots \\ E_n \end{bmatrix} = \begin{bmatrix} F_1^{e_1} - \int_0^1 f(\xi^{e_1}) N_1^{e_1} J^{e_1} A(\xi^{e_1}) d\xi^{e_1} \\ \vdots \\ F_1^{e_n} - \int_0^1 f(\xi^{e_n}) N_1^{e_n} J^{e_n} A(\xi^{e_n}) d\xi^{e_n} \end{bmatrix} \quad (24)$$

where $A_{ij} = \int_0^1 N_j \varepsilon(\xi^{e_i}) A(\xi^{e_i}) d\xi^{e_i}$.

$$N_j = \begin{cases} (1 - \xi^{e_i}) & \text{for } j = i \\ \xi^{e_i} & \text{for } j = i + 1 \\ 0 & \text{for all } j \neq i \text{ or } j \neq i + 1 \end{cases} \quad (25)$$

In addition, the boundary condition at the right end gives

$$E_{n+1} = P / [A(x=L)\varepsilon_{n+1}] \quad (26)$$

2.2 | Determination of A_{ij}

As shown in Equation (24), components of A_{ij} involve integration of terms involving the shape function and the measured strain values within each element. Full-field strain measurement techniques such as digital image correlation (DIC) provide strain values at a relatively dense set of discrete locations.^[22] Assuming that $\varepsilon(\xi^{e_i})$ are available at discrete points within an element, the integration in Equation (24) can be performed numerically (e.g. a trapezoidal rule). If the measured strain values do not coincide with nodal locations, the strains at these locations are determined by an

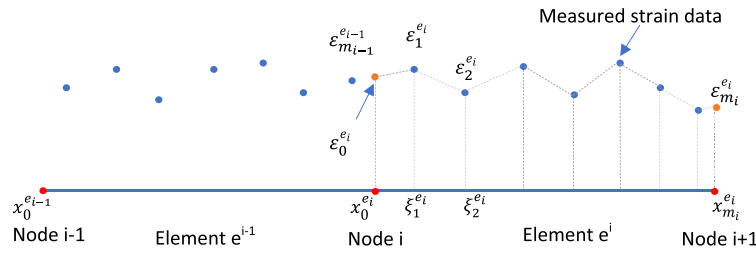


FIGURE 3 Schematic showing measured strain data locations with respect to the node positions

interpolation method. In this study, linear interpolation of the neighbouring strain values, as shown schematically in Figure 3, is implemented.

The trapezoidal numerical integration scheme used in this study is shown in Equation (27).[†]

$$\int_0^1 g_j(\xi^{e_i}) \epsilon(\xi^{e_i}) d\xi^{e_i} = \sum_{p=1}^{m_i-2} \left[g \left(\frac{\xi_p^{e_i} + \xi_{p+1}^{e_i}}{2} \right) \cdot \frac{\epsilon_p^{e_i} + \epsilon_{p+1}^{e_i}}{2} \right] + g \left(\frac{\xi_1^{e_i}}{2} \right) \frac{\epsilon_0^{e_i} + \epsilon_1^{e_i}}{2} + g \left(\frac{\xi_{m_i-1}^{e_i} + \xi_{m_i}^{e_i}}{2} \right) \frac{\epsilon_{m_i-1}^{e_i} + \epsilon_{m_i}^{e_i}}{2} \quad (27)$$

where $g_j(\xi^{e_i}) = N_j(\xi^{e_i}) A(\xi^{e_i})$.

3 | 1D MATERIAL PROPERTY IDENTIFICATION WITH GAUSSIAN NOISE

The Young's moduli obtained in this section are based on synthetically generated strain data with randomly distributed noise. The strain data are generated using a known spatial distribution of Young's modulus. Computational predictions for the Young's modulus distribution using strain data with and without noise are obtained for three different Young's modulus spatial distributions including (a) linear, (b) sinusoidal and (c) step change (Heaviside step function).

For each case, the authors included varying levels of random noise in the generated strain data to understand the effect of noise on modulus predictions. Other variables considered in the parametric study are (a) the number of elements and (b) the number of strain measurements within each element. Since cross-sectional area change has the same effect as a varying modulus for a 1D bar, the examples considered in this section assume a constant cross-sectional area. Additional results for quadratic variations in modulus with a constant, known body force, $f(x) = f_0$, are presented in Appendix A.

3.1 | Convergence criteria

To assess convergence, the authors considered element discretisation, number of strain data points and strain measurement variability as the relevant parameters. The basic parameters are defined as follows:

- a. discretisation element length, $L_e = L/N_e$, where N_e is the number of elements and L is the length of the specimen,
- b. number of strain data points per element, $N_d = M/N_e$, where M is the total number of strain data points along the length, L , and
- c. variability in each strain measurement, β_ϵ (standard deviation of noise in the strain data).

Since there are three parameters involved in the assessment of convergence, with β_ϵ oftentimes known a priori for the measurements, the goal is to determine a functional form for the lower bound on (N_d, L_e) that meets the convergence criterion for each β_ϵ .

[†]There are a range of methods that could be used to perform the integration shown in Equation (27). The authors have not evaluated other integration methods in this work.

3.1.1 | Convergence criterion for known solution, $E(x)$

For a given parameter set, (N_d, L_e) and fixed β_e , when values from the numerical modulus solution, $E_{FE}(x)$, satisfy the following inequality at N points along the length, L :

$$|E_{FE}(x_i) - E(x_i)| / E(x_i) \leq \Delta \quad \text{for all } i = 1, 2, \dots, N \quad (28)$$

where Δ is the user-defined convergence limit and $E(x_i)$ is the true modulus at coordinate location x_i .[‡] Equation (28) is used for all 1D material property identification studies where the functional form of $E(x)$ is known. As shown in Equation (28), the criterion ensures that the material property deviation at all node points is less than Δ at all node points the region of interest.

To determine the lower bound on (N_d, L_e) required for convergence with each β_e , 1D material property identification is performed for each discretisation, L_e , by varying N_d to determine the minimum number of strain measurements per element required to ensure convergence. By repeating 1D material property identification for various β_e , the effect of strain measurement noise on convergence is quantified. The set of lower bounds on $(N_d, L_e; \beta_e)$ for linear, sinusoidal and step-change distributions of Young's modulus are shown in Section 3.5.

Using the convergence criterion in Equation (28), parametric studies were performed to determine the regions within the parametric space (N_e, N_d, β_e) where the deviation, $\Delta < 0.04$. For the 1D case, closed-form solutions for strain are used to generate strain data for a known elastic modulus distribution.

When the true modulus distribution, $E(x)$, is known, then the level of discretisation required to meet the convergence criterion can be determined. Specifically, when L_e is reduced and all other parameters are held constant, the level of discretisation is defined for a specified N_d , with changes in N_d employed to determine the minimum required data density for convergence for each L_e . With regard to data density per element, Section 3.5.3 discusses the related issues of subset size, subset spacing, strain window size and speckle size.

3.1.2 | Convergence criterion for unknown modulus distribution, $E(x)$

When the numerical solution, $E(x)$, for a given parameter set, $(N_d, L_e; \beta_e)$, and the numerical solution, $E^*(x)$, for a given parameter set, $(N_d + \delta N_d, L_e + \delta L_e; \beta_e)$, satisfy the following inequality at N points along the length, L :

$$2|E_i(N_d + \delta N_d; L_e + \delta L_e, \beta_e) - E^*_i(N_d; L_e, \beta_e)| / |E_i(N_d + \delta N_d; L_e + \delta L_e, \beta_e) + E^*_i(N_d; L_e, \beta_e)| \leq \gamma \quad \text{for all } i = 1, 2, \dots, N \quad (29)$$

where γ is the user-defined convergence limit; then the solution is converged for the specified β_e . As shown in Equation (29), the normalised difference between the previous estimate and the current estimate for the material property must be less than a specified tolerance, γ .

3.2 | Linear distribution of Young's modulus

The linear distribution of Young's modulus considered in this work is given as

$$E = E_0 \left(1 + \frac{x}{L} \right) \quad (30)$$

where L is the length of the bar and E_0 is Young's modulus at $x=0$. Defining normalised strain as $\epsilon_N = \epsilon/\epsilon_o$ where $\epsilon_o = P/(A E_o)$. Figure 4 presents both Equation (30) and the predicted distribution of Young's modulus when solving

[‡]Here, x_i includes the points interior to the elements. In this work, $N = 4N_e + 1$, so 3 points in interior to the elements are selected in addition to the nodal locations.

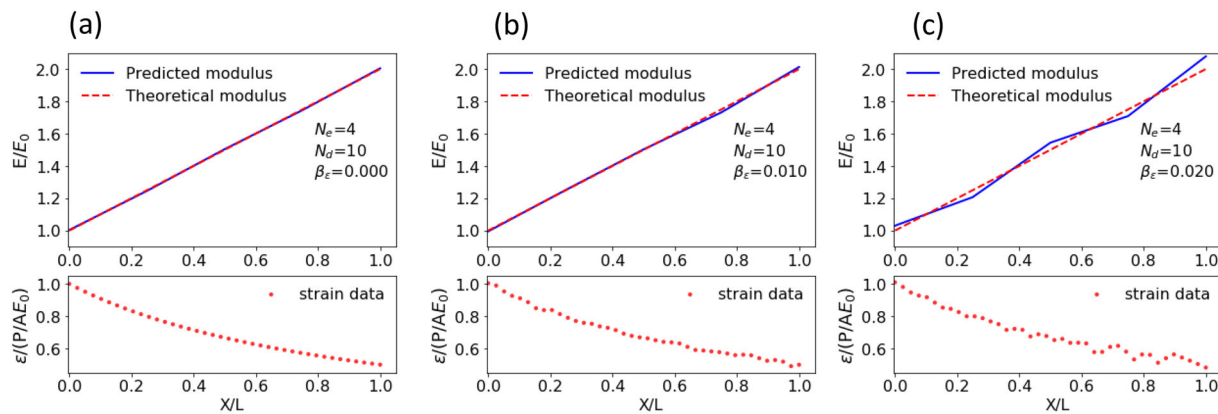


FIGURE 4 Theoretical and predicted $E(x)$ for $N_d = 10$, $L_e = L/4$ with (a) $\beta_\epsilon = 0$, (b) $\beta_\epsilon = 0.010$ and (c) $\beta_\epsilon = 0.020$

Equation (24) using $L_e = L/4$ (four elements) and $N_d = 10$ (10 strain data points per element) with (a) $\beta_\epsilon = 0$ (no noise), (b) $\beta_\epsilon = 0.010$ (Gaussian noise in the normalised strain with standard deviation of 0.010) and (c) $\beta_\epsilon = 0.020$.

From Figure 4a, it can be observed that the predicted modulus distribution coincides with the true modulus when there is no noise in the strain data, the expected result since each element shape function is linear. As shown in Figures 4b,c, as noise in the strain data increases, the predicted modulus begins to oscillate about the exact solution, even though 10 strain data points are used in each element. A discussion of the required parameters to obtain a convergent solution for a linearly varying $E(x)$ defined in Equation (30) is given in Section 3.5.1. For $\beta_\epsilon = 0.020$, Figure 5 shows the effect of increased data density, N_d , on the predicted modulus. Inspection of Figure 5 shows excellent agreement with the theoretical $E(x)$ distribution with $N_d = 80$ when $L_e = L/4$.

3.3 | Sinusoidal distribution of Young's modulus

To represent the more difficult case where Young's modulus is varying cyclically, the authors performed the 1D material property identification procedure using the sinusoidal distribution in Young's modulus represented by Equation (31).

$$E = E_0 \left(2 + \sin \left(2\pi k \frac{x}{L} \right) \right) \tag{31}$$

where k is the wavenumber and $2\pi/k$ is the wavelength of the sinusoidal variation in $E(x)$ and x is length along the axis in Figure 1. Three different values of k are considered in this work; $k = 0.5$, $k = 2.5$ and $k = 5.0$. For each value of k , strain data are generated along the length of the specimen for use in assessing the accuracy of the Young's modulus predictions using Equation (24).

For $E(x)$ varying sinusoidally with $k = 0.5$, exact strain data and $N_d = 10$, Figure 6a–c compares the exact $E(x)$ distribution to the predicted distribution for $L_e = L/2$, $L/10$ and $L/20$, respectively. Similarly, when $k = 2.5$ and $N_d = 10$, Figure 7a–c compares the exact $E(x)$ distribution to the predicted distribution for $L_e = L/10$, $L/20$ and $L/40$, respectively. Finally, when $k = 5.0$ and $N_d = 10$, Figure 8a–c compares the exact $E(x)$ distribution to the predicted distribution for $L_e = L/20$, $L/40$ and $L/80$, respectively.

As shown in Figures 6–8, as the sinusoidal frequency of $E(x)$ increases, the element size must decrease while maintaining the same number of strain data points per element to predict $E(x)$ more accurately. It should also be noted that the results in Figure 6a show the minimum number of elements required to predict the modulus with reasonable accuracy given by

$$N_e > 2k \tag{32}$$

Equation (32) is another form of the Nyquist frequency limit used to define the required sample frequency to minimally reconstruct varying signals with wavenumber k . Further inspection of Figures 6c and 7c show that they are somewhat oversampled relative the Nyquist limit and hence are better approximated.

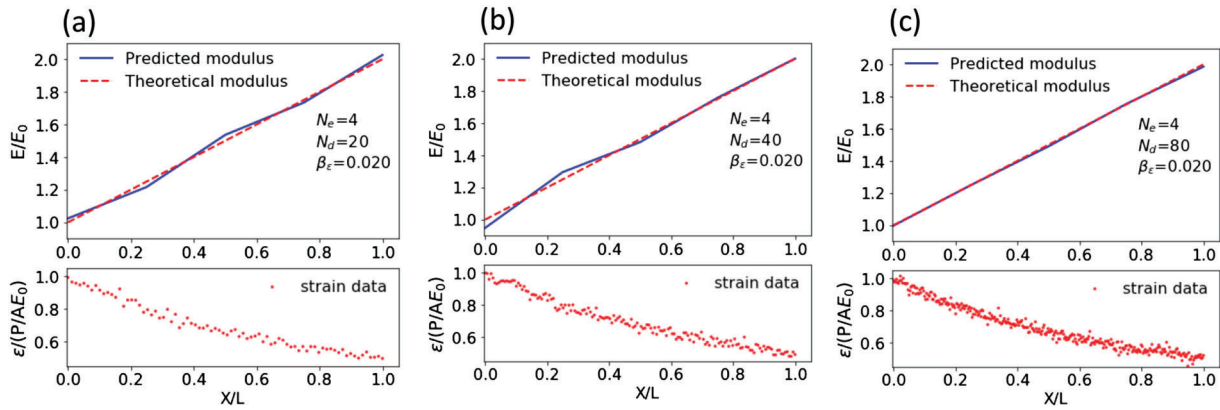


FIGURE 5 Theoretical and predicted $E(x)$ for $L_e = L/4$, $\beta_e = 0.020$ and (a) $N_d = 20$, (b) $N_d = 40$ and (c) $N_d = 80$

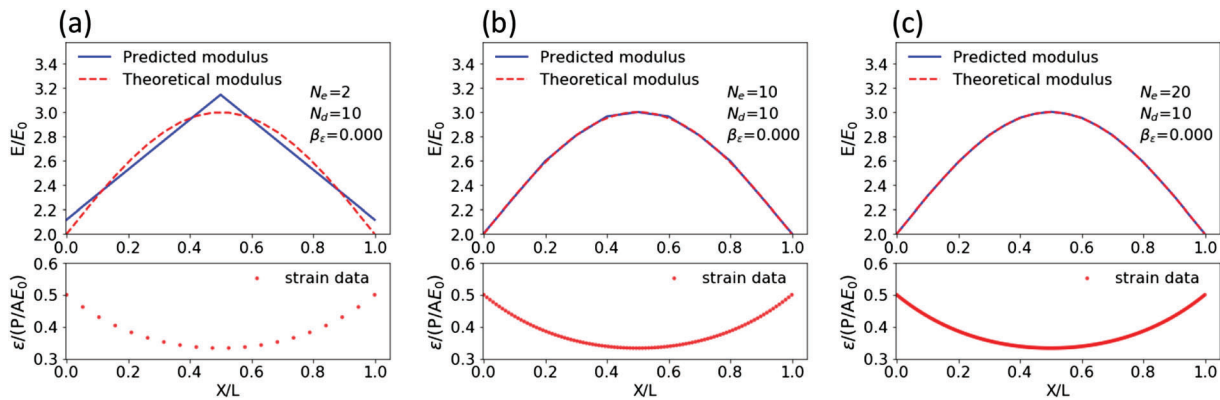


FIGURE 6 Predicted $E(x)$ using Equation (24) and exact $E(x)$ using Equation (31), along with exact strain data for each case with $k = 0.5$, $\beta_e = 0$, $N_d = 10$ and (a) $L_e = L/2$, (b) $L_e = L/10$ and (c) $L_e = L/20$

For the highest wavenumber case, $k = 5.0$, $N_d = 10$ and $L_e = L/80$, Figure 9a–c shows the effect of noise on the predicted modulus for (a) $\beta_e = 0.005$, (b) $\beta_e = 0.010$ and (c) $\beta_e = 0.020$, respectively. Similar to the cases for the linear modulus distributions, increasing noise levels result in increasing variability in $E(x)$, though the general form is consistent with the exact modulus distribution.

For $k = 5.0$, $L_e = L/80$ and $\beta_e = 0.020$, the effect of increased data density, N_d , on the predicted $E(x)$ distribution is shown in Figure 10. Section 3.5 provides a discussion of the required parameters to obtain a convergent solution.

3.4 | Step change in Young's modulus (Heaviside distribution)

The most challenging situation involves step changes in Young's modulus distribution, as given by Equation (33).

$$E(x) = E_0 \begin{cases} 2.00 : 0.00 \leq \frac{x}{L} < 0.25 \\ 1.75 : 0.25 \leq \frac{x}{L} < 0.50 \\ 1.50 : 0.50 \leq \frac{x}{L} < 0.75 \\ 1.25 : 0.75 \leq \frac{x}{L} \leq 1.00 \end{cases} \quad (33)$$

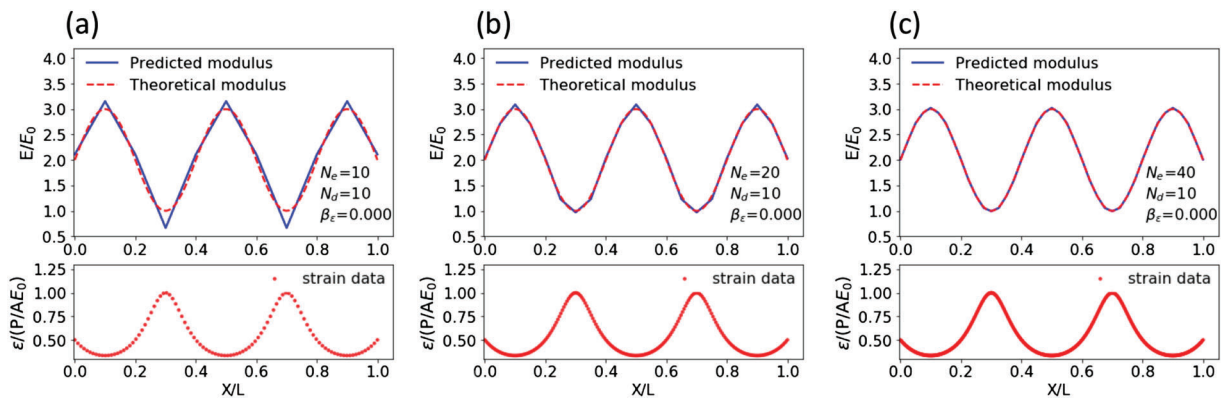


FIGURE 7 Predicted $E(x)$ using Equation (24) and exact $E(x)$ using Equation (31), along with exact strain data for each case with $k = 2.5$, $\beta_e = 0$, $N_d = 10$ and (a) $L_e = L/10$, (b) $L_e = L/20$ and (c) $L_e = L/40$

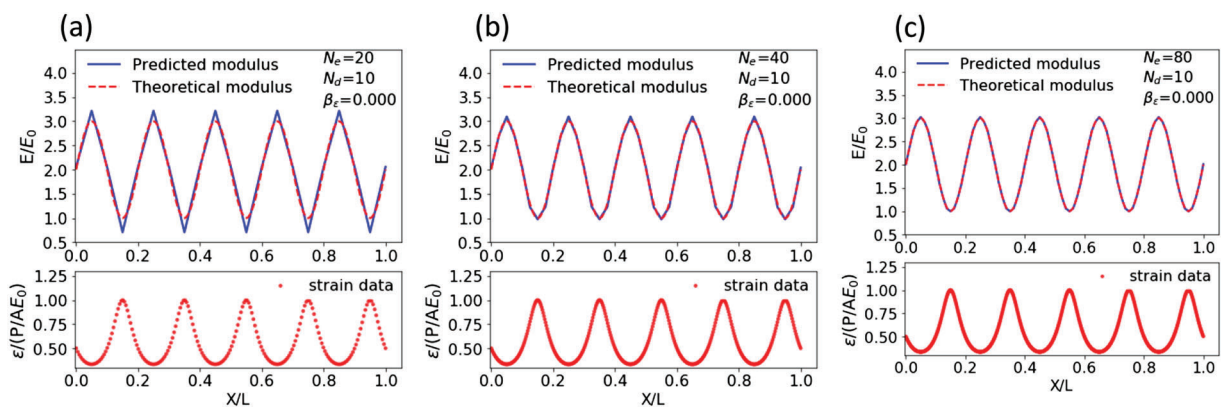


FIGURE 8 Predicted $E(x)$ using Equation (24) and exact $E(x)$ using Equation (31), along with exact strain data for each case with $k = 5.0$, $\beta_e = 0$, $N_d = 10$ and (a) $L_e = L/20$, (b) $L_e = L/40$ and (c) $L_e = L/80$

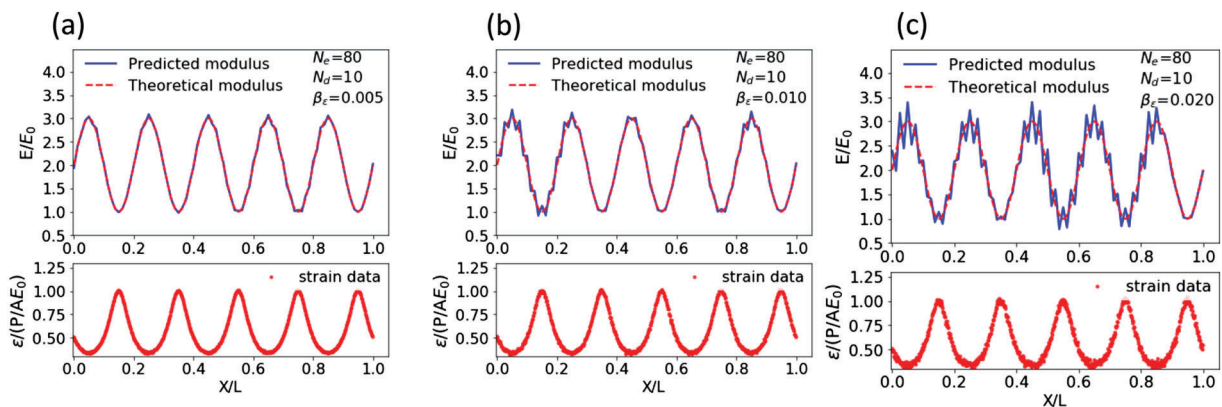


FIGURE 9 Predicted $E(x)$ using Equation (24) and exact $E(x)$ using Equation (31), along with strain data for each case with $k = 5.0$, $L_e = L/80$, $N_d = 10$ and (a) $\beta_e = 0.005$, (b) $\beta_e = 0.01$ and (c) $\beta_e = 0.02$, respectively

Situations such as given in Equation (33) are known to introduce spurious oscillations in the solution due to the presence of step changes that are inconsistent with the requirement for continuous derivatives in the domain (see Equation 3). Even so, the authors performed 1D material property identification procedure to determine how sensitive the current formulation is to the discontinuous $E(x)$ representation.

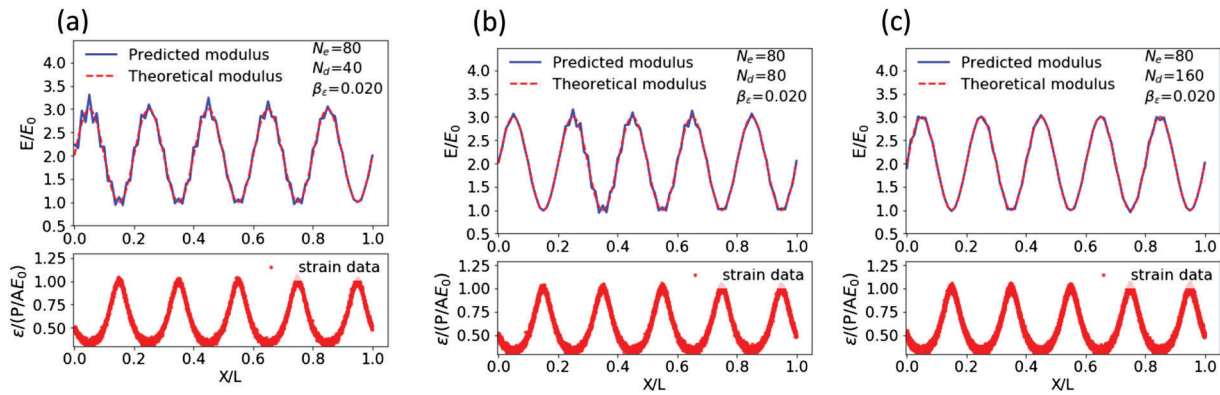


FIGURE 10 Predicted $E(x)$ using Equation (24) and exact $E(x)$ using Equation (31), along with strain data for each case with $k = 5.0$, $L_e = L/80$, $\beta_\epsilon = 0.02$ and (a) $N_d = 40$, (b) $N_d = 80$ and (c) $N_d = 160$, respectively

For exact ϵ_N data in the continuous regions, Figure 11 compares the predicted Young's modulus using Equation (24) to the exact distribution for $N_d = 10$ and (a) $L_e = L/25$, (b) $L_e = L/50$ and (c) $L_e = L/100$, respectively. As shown in Figure 11, the discontinuities created oscillations that propagated throughout the domain, increasing in frequency with the number of elements used to represent the modulus distribution.[§]

To show the effect of strain noise on predictions, for $L_e = L/50$, $N_d = 10$, Figure 12 compares the predicted and theoretical $E(x)$ distributions for (a) $\beta_\epsilon = 0.005$, (b) $\beta_\epsilon = 0.010$ and (c) $\beta_\epsilon = 0.020$, respectively. Inspection of the results in Figure 12 confirms that the addition of noise does not eliminate the oscillations. Interestingly, for the highest levels of noise in the strain data, the data in Figure 12c show that the elevated noise level tends to obscure the strain discontinuity at the step changes, somewhat muting the oscillatory nature of the model predictions and marginally improving the comparison to the exact $E(x)$ distribution.

Finally, the theoretical ϵ_N strain data with additive noise was modified using a Butterworth filter to smooth the discontinuities.^{[23]¶} Using the filtered strain data with $N_d = 10$ and $L_e = L/50$, Figure 13a–c compares the predictions to the exact $E(x)$ distribution for filtering with cut-off frequency[#] of (a) 20, (b) 10 and (c) 5, respectively. Inspection of Figure 13 shows that, for small levels of smoothing, most of the oscillations have been removed and the general shape of the predictions matches the theoretical distribution. As the amount of smoothing increases, the predictions do not match the exact $E(x)$ distribution.

3.5 | Parametric study

Visual inspection of Figures 5–13 is oftentimes used to provide a general impression of the quality of agreement between computational and exact modulus values. For example, the computational predictions in Figure 10c clearly have differences at some points, but the overall trends are well represented for this data density and discretisation, which may be sufficient for some applications. In cases where quantitative comparisons are desirable, the convergence criteria in Section 3.1 are employed to define a set of parameters that ensure the computational predictions meet specific requirements over the domain.

For known $E(x)$, Equation (28) is used to define lower bound combinations of data density (N_d) and discretisation (L_e) for a given variability in the strain data (β_ϵ) that ensure the difference in the modulus distribution on the domain meets a specified tolerance, Δ . In the remainder of this section, the lower bound results obtained from extensive 1D material property identification procedures are presented for linear and sinusoidal variations in $E(x)$ with a range of β_ϵ variability in the strain data.

[§]An approach that the authors used effectively is to remove the step change and incorporate a relatively steep continuous change in modulus at each discontinuity. Though not shown here, provided there are strain data points within the short continuous region to reconstruct the modulus in this region, the modification minimises oscillations.

[¶]The order of the filter is chosen as 2.

[#]The cut-off frequency is the normalised special frequency given by $2\pi/\lambda$ where λ is the wavelength/ L .

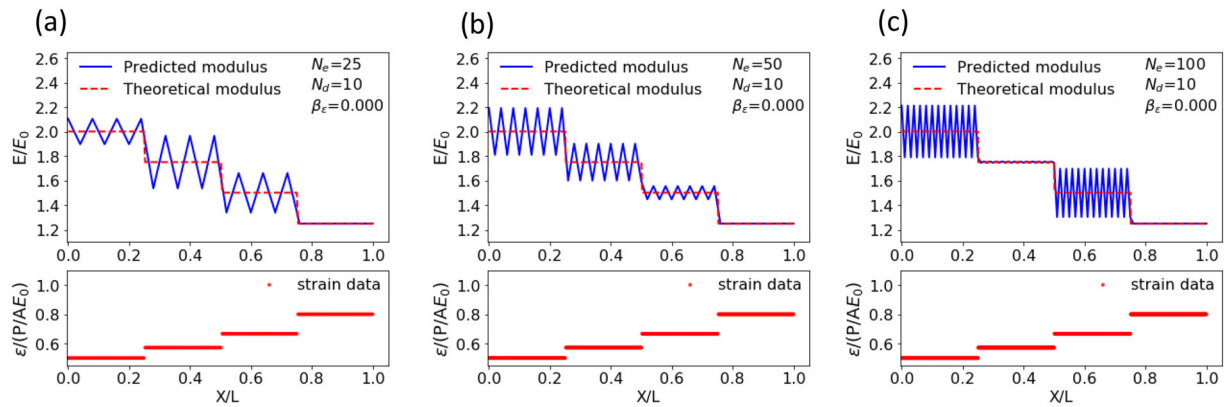


FIGURE 11 Predicted $E(x)$ using Equation (24) and exact $E(x)$ using Equation (33), along with strain data for each case with $\beta_\epsilon = 0$, $N_d = 10$ and (a) $L_e = L/25$, (b) $L_e = L/50$ and (c) $L_e = L/100$, respectively

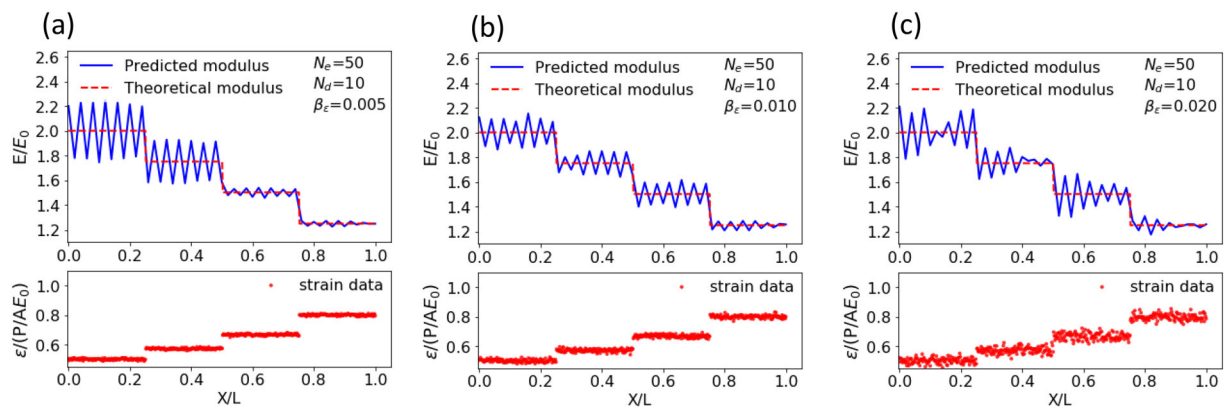


FIGURE 12 Predicted $E(x)$ using Equation (24) and exact $E(x)$ using Equation (33), along with strain data for each case with $N_d = 10$, $L_e = L/40$ and (a) $\beta_\epsilon = 0.005$ (b) $\beta_\epsilon = 0.010$ and (c) $\beta_\epsilon = 0.020$, respectively

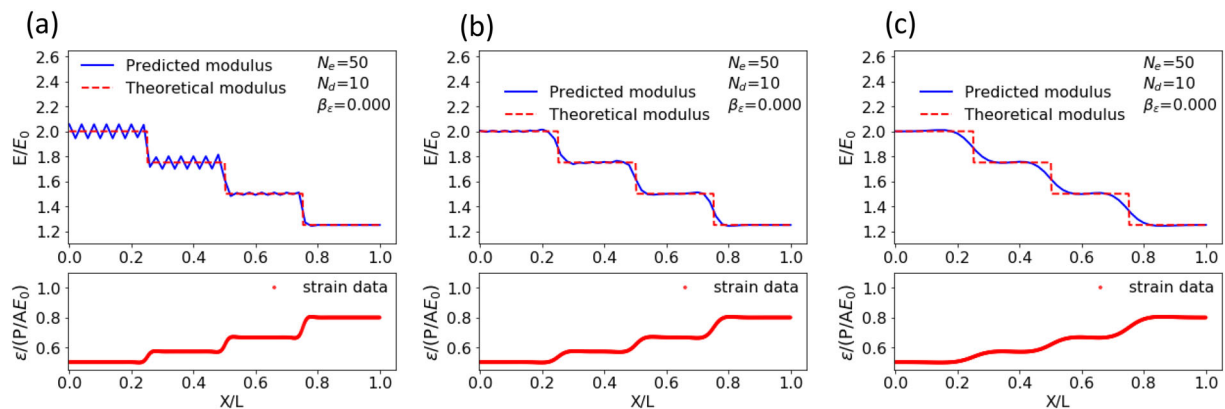


FIGURE 13 Predicted $E(x)$ using Equation (24) and exact $E(x)$ using Equation (33), along with strain data for each case with $N_d = 10$, $L_e = L/50$, $\beta_\epsilon = 0$ and Butterworth smoothing with normalised cut-off frequency ($2\pi/\lambda$ where λ is the wavelength/ L) of (a) 20, (b) 10 and (c) 5, respectively

3.5.1 | Convergence parameters for linearly varying $E(x)$

The effect of parameters such as the number of elements in the FE model (N_e), number of strain data points per element (N_d) and noise in the generated data (standard deviation of β_ϵ) for a linearly varying modulus is presented in

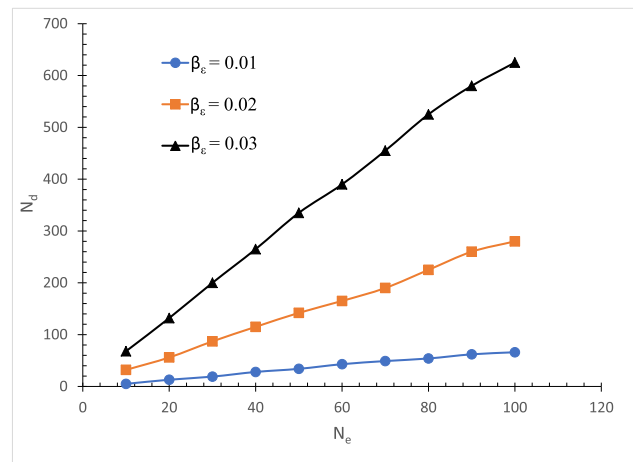


FIGURE 14 Plot of N_d versus N_e for selected values of β_e and linear variation in Young's modulus

Figure 14. The standard error limit for these convergence studies is $\Delta = 0.04$ or 4% to determine the minimum number of elements.^{**} The plot shown in Figure 14 can also be interpreted as the boundary in the parameter space (N_e and N_d) where the choice of a set of parameters above the curve results in a standard error of the predicted modulus to be lower than 4% of the true modulus.

The strain data used in the 1D material property identification procedure were generated using Equation (30) with varying levels of random noise added to the strain data, including the zero-noise condition. From Figure 14, it can be observed that N_d increases linearly with N_e for $\beta_e > 0$. The minimum value of N_d is observed to increase quadratically with increase in β_e . Hence, as β_e increases, a larger number of strain data per element is required for convergence.^{††}

3.5.2 | Convergence parameters for sinusoidally varying $E(x)$

For sinusoidally varying $E(x)$, two different wavenumbers (spatial frequencies $k = 2\pi/\lambda$, $\lambda = \text{wavelength}/L$) are selected ($k = 2.5$ and 5). The effect of N_e , N_d and β_e for $k = 2.5$ and 5 are shown in Figures 15 and 16, respectively. The value of N_e separating Regions I and II is found to increase with wavenumber, k . In Region II, the dependence of N_d on N_e and β_e is like results shown in Figures 14 for linearly varying $E(x)$. In Region I, the minimum value of N_d appears to increase exponentially with decreasing N_e . When $N_e < 20$ for $k = 2.5$ and $N_e < 55$ for $k = 5.0$, for $\Delta = 0.04$, the solutions do not converge, regardless of the element data density, N_d . Though not shown, increasing Δ will decrease Region 1, with a secondary lower limit on N_e corresponding to the Nyquist limit shown in Equation (32).

3.5.3 | Discussion and practical implications

To obtain the necessary data density, N_d , for accurate reconstruction of the modulus distribution, the relationship between an appropriate DIC subset size, DIC strain window size, FE element size and data density should be discussed. Figure 17 shows the concept graphically for a specific example where five strain data points are used per finite element. As shown in Figure 17, for a discrete element size, L_e , when five strain data points are input for each element with a 50% overlap of strain windows, then the strain window size is $L_e/2$, with a spacing between window centres of $L_e/4$. Assuming that each strain window uses a 5×5 set of displacement data to determine the strains at the five points (\bullet) shown in Figure 18, when a 50% overlap of subsets also is used to obtain the displacement data in the strain window, then each subset size would be $L_e/2$ with a spacing between subset centres of $L_e/4$.

The parametric studies performed earlier in this section employed generated strain with Equation (28) to assess convergence when the true distribution of the elastic modulus is known a priori. In real-world applications, such as the

^{**}Additional results for different values of the standard error in predicted $E(x)$ is shown in Appendix A.

^{††}For $\beta_e = 0$, the minimum value of N_d is two for all values of N_e since the shape function is linear and the underlying $E(x)$ distribution is also linear.

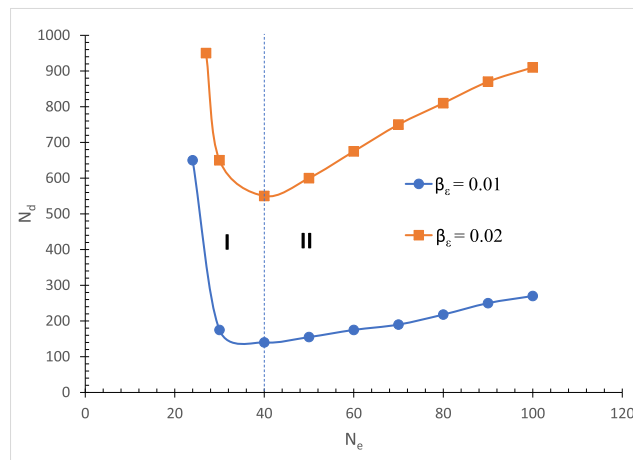


FIGURE 15 Plot of N_d versus N_e for selected values of β_e and sinusoidal variation in Young's modulus with $k = 2.5$

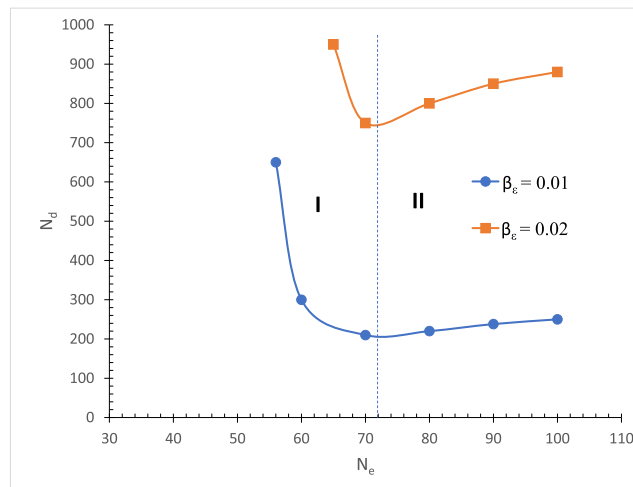


FIGURE 16 Plot of N_d versus N_e for selected values of β_e and sinusoidal variation in Young's modulus with $k = 5$

one to be presented in Section 4, the underlying distribution of the material properties is unknown. In such cases, the results in Figures 14–16 can serve to identify potential combinations of N_d and N_e for a known β_e that would be appropriate as a starting point for convergence studies.

As an example, suppose that a specimen of length, L , with an approximately linear distribution in modulus is imaged and strain data are acquired at 1000 points along the length with strains ranging from 500 to 3000 $\mu\epsilon$ and baseline strain variability of 25 $\mu\epsilon$. In this case, the average $\beta_e \approx 0.03$. Using the results in Figure 14, only a few elements can be used to obtain results with reasonable accuracy. For example, suppose discretisation into $N_e = 20$ elements is desirable. In this case, $N_d^{\max} = 1000/20 = 50$. However, according to Figure 14, $N_d \geq 130$ is required to meet the convergence criterion, which is not achievable. Based on Figure 14, the maximum number of elements that can be used for convergence is $N_e \approx 12$, which requires $N_d \approx 80$, a value that is slightly less than the maximum achievable with 1000 data points ($M/N_e \approx 83$).

Following the previous discussion and considering the geometry in Figure 17, the length L is discretised into 12 elements with $L_e = L/12$ and a distance of $L/960$ between each of the 80 strain data points. Considering a 5×5 strain window with 50% overlap of subsets, each subset has dimension $L/1920$ so that five subsets span each strain window. If each subset is imaged onto a 20×20 pixel area, the transverse magnification factor, $M_T = 38,400/L$ in units of pixels/unit length. Finally, if the specimen length is 20 mm, then $M_T = 1920$ pixels/mm and each fully resolved speckle (a speckle spanning a 3×3 pixel area) is 1.5 μm in physical size, requiring microscope imaging with a digital camera that has a $38,400 \times 38,400$ array.

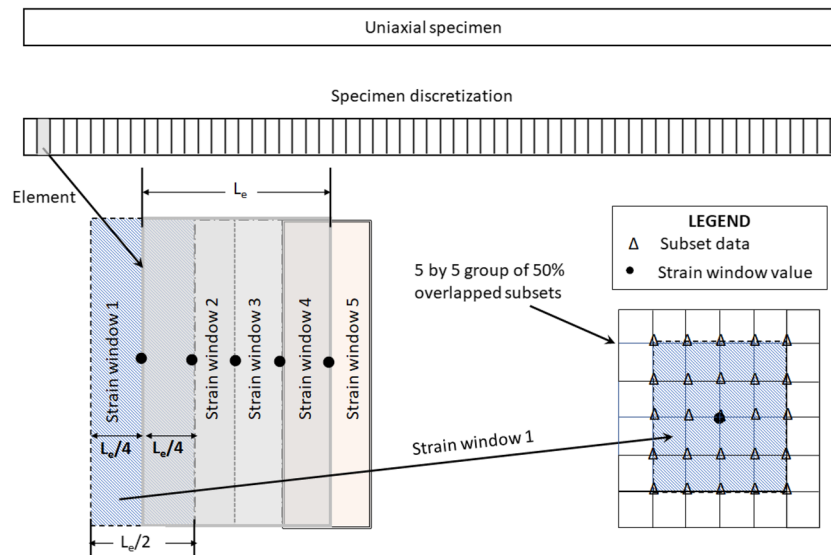


FIGURE 17 Schematic of uniaxial specimen discretisation with FE element size L_e and overlapping DIC strain windows to obtain five strain data points per elements. Each strain data point is determined using subset-based values from a 5×5 group that have 50% overlaps. Triangles denote locations for subset strain measurements. Dot denotes strain window strain value using all subset data in the window and centre-weighted Gaussian average of subset measurements

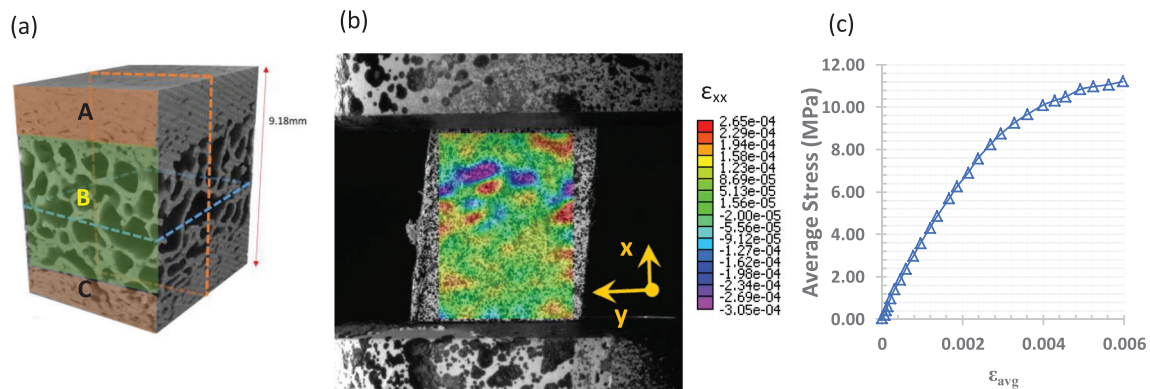


FIGURE 18 (a) Micro-CT scan image of the bone sample, (b) 2D-DIC measurements of axial strain field for $\sigma = 4$ MPa, (c) average compression stress versus axial strain data for specimen

As an additional example consider the sinusoidal variation case with $k = 2.5$. As shown in Figure 15, when $\beta_e = 0.03$, the results are not even on the graph since $N_d > 1000$ is predicted to be required for the optimal number of elements. Assuming that strain errors can be reduced so that $\beta_e = 0.02$, Figure 15 suggests that when $N_e = 50$, then $N_d = 550$ is required to achieve convergence with $\Delta = 0.04$. This combination corresponds to having 27,500 strain data points along the length of the specimen, a data density that is nearly $30\times$ larger than discussed for the linear modulus variation example. Even if a 50-MP camera sensor were available to image the entire length, L , this would only result in ≈ 7000 data points along the specimen length, woefully short of the required number, without considering the issues associated with subset and speckle size noted previously. One option would be to obtain high-resolution images of sequential lengths ϕL , where $\phi < 1$, that span the entire length from 0 to L and can individually meet the required convergence criterion. In this case, loading and deformations in each length segment must remain stable when the images are acquired.

4 | MODULUS PREDICTIONS WITH EXPERIMENTAL DATA

To assess the methodology using full-field DIC experimental data, recent measurements by two of the authors^[24] are employed. In their work, Weerasooriya and Alexander performed axial compression experiments on the small bone sample shown in Figure 18a. As shown in Figure 18, the specimen has a length of 9.18 mm, width of 7.3 mm and a cross-sectional area of 70.95 mm²; details of the experimental setup and DIC hardware used are given in literature.^[24] As noted in literature,^[24] inspection of the micro-CT scan shown in Figure 18a indicates the specimen has a well-defined variation in bone structure along the vertical length that is nominally similar for vertical x–y and y–z cross sections. Based on these observations, the authors^[24] assumed the specimen structure (i.e. bone volume fraction, V_f) is only a function of the position along the vertical direction (i.e. the x-direction in Figure 18a) and is independent of both transverse directions. The authors^[24] then performed 2D-DIC measurements on a visible x–y surface to obtain surface strain fields during mechanical compression loading. The full-field axial strain measurements for an axial stress, $\sigma = 4$ MPa, are shown in Figure 18b, and the quasi-static average stress versus average strain results are shown in Figure 18c.^[24]

In this study, the images obtained previously^[24] are analysed using VIC-2D^[25] with the analysis parameters given in Table 1 to obtain 1018 strain data points horizontally and 1415 strain data points vertically.^{‡‡} Due to the relatively coarse nature of the speckle pattern in the specimen, a relatively large subset size is used, which has the effect of smoothing spatial gradients in the measured data (see literature^[6] for speckle size and subset size requirements). As shown in Figure 18a, variations in bone density within the specimen required the authors to use two different sets of DIC parameters within zones (A, B, C); the subset size in each zone is shown in Table 1, with each subset sufficiently large to span six intensity transitions in each direction.^{[6]§§}

Inspection of Figure 18b confirms that the axial compressive strain field is heterogeneous, which is consistent with the CT scan image in Figure 18a that clearly shows the bone volume fraction is higher in Zones A and C. Detailed analysis of the CT images using a representative volume element (RVE) demonstrated that bone density is nominally uniform in the Y and Z directions, varying from top to bottom (X-direction).^[24] Based on these measurements, it is reasonable to assume the specimen deformation in the X direction could be predicted using a 1D model of an axially heterogeneous material, with the axial strain at each vertical position obtained by averaging the measured axial strains across the width of the specimen.^[24,27]

The recalculated average strain values across the width of specimen in the central region using 2D-DIC and the parameters in Table 1 for different load levels are shown in Figure 19. Though not shown in Figure 19, analysis of the strain data obtained along the entire length of the specimen demonstrated that the measured strains near the top and bottom boundaries of the sample were nearly zero for all load levels, primarily due to frictional interaction of the loading platen surfaces, resulting in a complex localised stress state and constrained local deformations. Thus, only the strain data from the central 80% of the specimen are shown in Figure 19 and used in the 1D material property identification procedure, with data from the upper 10% and lower 10% of the length excluded from the analysis.

TABLE 1 DIC parameters selected for three zones in the area of interest shown in Figure 18

DIC parameters	Zones A and C	Zone B
DIC software	VIC-3D, Version 8	VIC-3D, Version 8
Image filtering	Gaussian filter with a 3×3 pixel kernel	Gaussian filter with a 3×3 pixel kernel
Subset size	75 pixels/487 μm	151 pixels/980 μm
Step size	1 pixel/6.5 μm	1 pixel/6.5 μm
Subset shape function	Affine	Affine
Matching criterion	Zero-normalised sum of square differences (ZNSSD)	ZNSSD
Interpolant	Bi-cubic spline	Bi-cubic spline
Strain window	5 data points	5 data points
Virtual strain gauge size ^a	79 pixels/513 μm	155 pixels/1006 μm
Strain formulation	Green–Lagrange	Green–Lagrange
Strain noise floor ^b	40 $\mu\epsilon$	30 $\mu\epsilon$

^aThe virtual gauge length is computed from equation 7.2 in the DIC Good Practices Guide.^[26]

^bBaseline analysis is performed by taking speckle images of the sample before loading and performing DIC for calculating variability in the measurements.

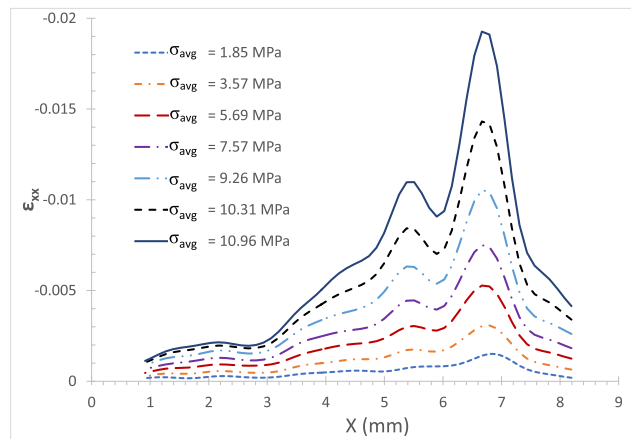


FIGURE 19 Average measured axial strain data along length of specimen, $\varepsilon_{xx}(x)$, versus average axial stress, σ_{avg}

4.1 | Predictions of Young's modulus for elastic range

Prior to predicting the 1D distribution of Young's modulus, observations regarding the measured strain data are described. Firstly, baseline analysis of specimen images using the parameters specified in Table 1 indicated that variability range for the strain measurements is $\pm 40 \mu\epsilon$. Secondly, since measured axial strains during the early stages of loading are of the order of $400 \mu\epsilon$ or less, the signal-to-noise ratio is less than 10, and β_e is near 0.10. In such cases, to obtain accurate predictions for $E(x)$, the required N_d for a given N_e will be quite high, even for a small number of elements. Since the maximum number of strain data is fixed by the vertical pixel dimensions of the camera (i.e. $M < 1415$ pixels), for $\sigma_{avg} < 0.50$ MPa where for average strain is less than $400 \mu\epsilon$, variability in the predicted moduli is expected to be higher than is seen at elevated stress values.

To predict Young's modulus within the nominally elastic strain range, 1D material property identification procedure are performed for the range $1000 \mu\epsilon \leq \delta/L = \varepsilon_{engr} \leq 2000 \mu\epsilon$, which corresponds to the range $4 \text{ MPa} \leq \sigma_{avg} \leq 6 \text{ MPa}$. Comparison of the measured strain distributions in Figure 19 to our previous analysis predictions shows the strain fields in the early stages are qualitatively similar to a quadratic function. Based on the convergence study and results shown in Figure A5, preliminary values for N_d and L_e can be estimated for the data density available, which is a maximum of ≈ 1100 data points along the central portion of the specimen. Thus, if $\beta_e = 0.01$, then $N_e = 40$ corresponds to $N_d \approx 25$.

Since higher discretisation is preferred to reconstruct any variations in modulus, the authors initiated the optimisation process with $N_e = 10$, $N_d \approx 110$ and performed 1D material property identification procedure by increasing N_e and continually selecting the maximum N_d available. Progress towards convergence in the predicted moduli for the elastic range is shown in Figure 20. Using Equation (29) with $\gamma = 0.04$ to check convergence of the results shown in Figure 20,[¶] results indicate that the minimum N_e satisfying the convergence criterion is $N_e = 50$. The predicted elastic moduli for three different load levels within the elastic range using 50 elements are shown in Figure 21, along with the independently estimated modulus distribution from ref. [24].

As shown in Figure 21, the elastic modulus predicted using the three load levels are nearly the same, indicating the presence of elastic behaviour within the load levels considered. In addition, the predictions in this study are in good agreement with previous estimates obtained by Alexander et al.^[24]

4.2 | Prediction of secant modulus distributions

For loading beyond the linear elastic region, Equation (24) is used incrementally to determine the local secant modulus and its evolution with increasing stress. Following the same procedures as described previously, the authors performed

[¶]Higher number of elements is required for obtaining a converged solution due to high-frequency components in the modulus variation in the sample. The explanation for the lower N_d is due to smoothing in the data as a result of averaging as explained in Section 4.

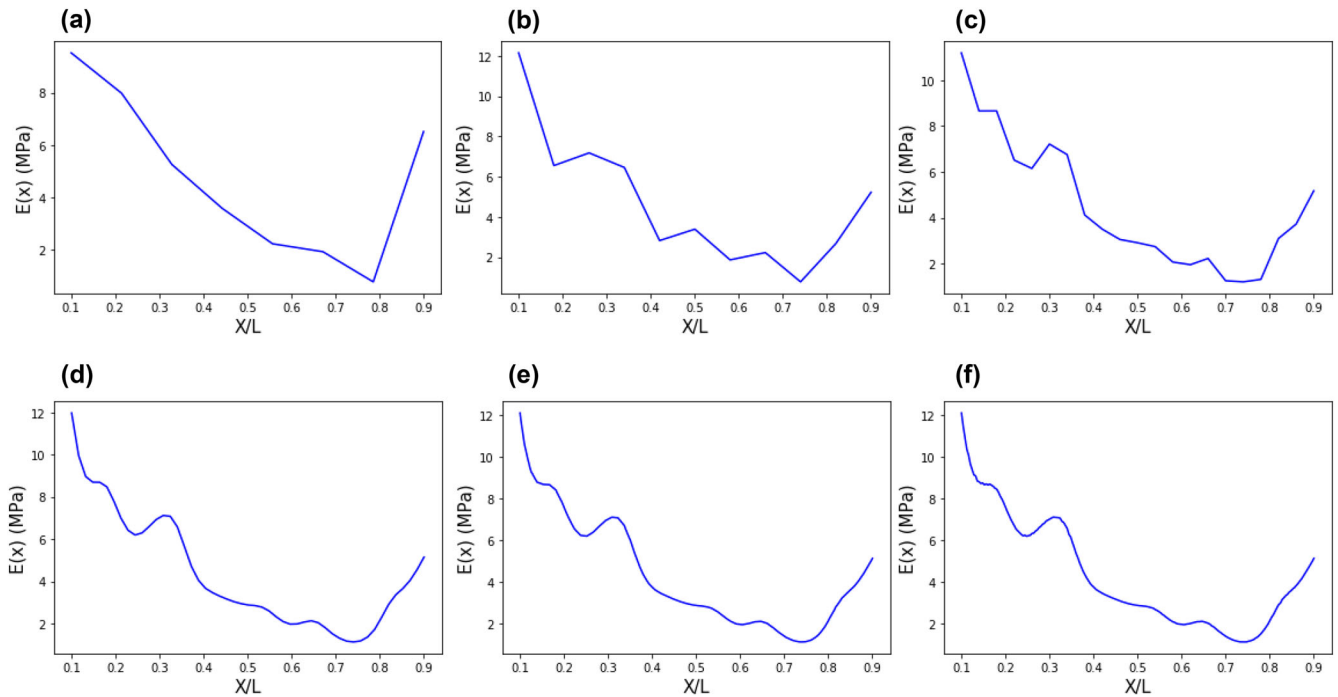


FIGURE 20 Distribution for predicted $E(x)$ using Equation (24) with (a) $N_e = 7, N_d = 162$, (b) $N_e = 10, N_d = 114$, (c) $N_e = 20, N_d = 57$, (d) $N_e = 50, N_d = 23$ (e) $N_e = 200, N_d = 6$, and (f) $N_e = 400, N_d = 3$. Specimen length, $L = 9.18$ mm

additional 1D material property identification procedure for higher loads to determine the evolution of the local secant modulus. Figure 22 presents the modulus distributions obtained using Equation (24) for the linear elastic case where $\sigma = 5.69$ MPa and the local secant modulus, E_s , through incremental analysis for stress values beyond the linear elastic range.

Inspection of the results in Figure 22 highlights the reduction in E_s with increasing stress that is indicative of softening behaviour in the bone material.

4.3 | Reconstruction of local stress–strain response

The distributions $E(x)$ and $E_s(x)$ can be used to estimate local slopes of the stress–strain data and then used to reconstruct the σ_{avg} versus ϵ_{avg} response of the bone material. Figure 23 shows the reconstructed σ_{avg} versus ϵ_{avg} response of the bone material for four locations along the length of the specimen.

The stress–strain relationship shows the difference in the elastic modulus, yield point and the hardening parameters at different locations of the sample. Thus, the capability of the model in calculating the constitutive relationship is illustrated in Figure 23.

5 | DISCUSSION OF RESULTS

First, the current finite element model uses small strain assumptions during the derivation (i.e. $\epsilon_{axial} \approx du/dx$). Thus, the approach is nominally limited to maximum strains of the order of 0.10, which is almost always the case when considering the elastic response of a material. If this is a concern, the model could be modified to include the effects of larger strains considered in the developments. Another option would be to perform the analyses incrementally, with each increment of strain meeting the current model’s strain requirements. To utilise the latter approach, the experiment should be performed in a way that provides sufficient strain data for each increment to ensure convergence in the 1D material property identification procedure.

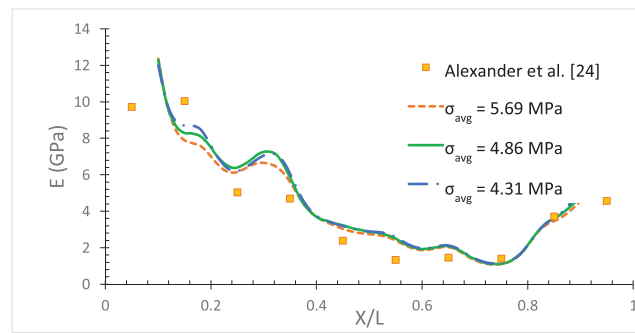


FIGURE 21 Elastic modulus predicted using inverse method for three different load levels within the elastic limit (50 elements were used in the inverse analysis)

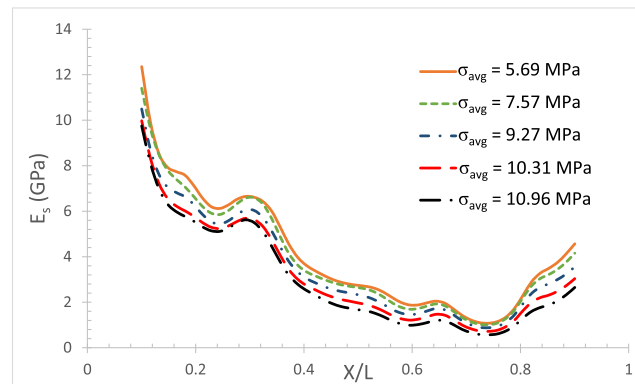


FIGURE 22 Predicted distributions using Equation (24) for $E(x)$ in linear elastic case with $\sigma = 5.69$ MPa and incremental analysis to obtain secant modulus, $E_s(x)$, for applied stresses beyond the linear elastic range

Inspection of the results for the experimental data shown in Figure 20 indicates that, as the element size and data density continue to decrease beyond the first combination satisfying the convergence criteria, solutions using Equation (24) continue to meet the convergence criteria, at least for the range studied in this application. Even when the data density decreases to three measurements per element, the solution continues to be convergent. The effect of various parameters, including further reductions in data density, increases in measurement error, β_e , and changes in the level of discretisation, has not been quantified in this study.

As noted in Section 3.5.3, results in Section 3.5 were used to provide initial estimates for (N_d, N_e) based on the use of Equation (28) to assess convergence. Though conceptually helpful, the fact that the least squares criterion used to assess convergence for known $E(x)$ is quite different from the incremental approach in Equation (29) used to determine convergence for an unknown $E(x)$ distribution makes it less clear how close to the underlying $E(x)$ the results are upon convergence. In this case, the initial estimates ($N_e = 40, N_d = 25$) for a known quadratic distribution with $\beta_e = 0.01$ are reasonably close to the parameter set that resulted in convergence ($N_e = 50, N_d = 22$) using Equation (29).

The convergence study shows that mesh density (N_e) of the FE analysis for material property determination depends strongly on measurement parameters (N_d) and noise in the data (β_e). As discussed in Section 3.5.3 and shown in Figure 17, there is a direct relationship between parameters N_d, N_e and subset size, step size and speckle size for DIC-based measurements, with β_e dependent upon intensity pattern noise and subset size. Though data obtained with smaller subsets are more capable of capturing strain gradients, there will be increased variability in the strain data due to inherent variability in the pixel intensity data.

Using an incremental approach to extend the range of applicability of Equation (24) is reasonable for simple applications such as uniaxial compression or tension where the total strain versus average stress are the quantities of interest. For applications where (a) the stress state and boundary conditions are more complex (e.g. plane stress or plane strain) and (b) multiple material parameters are to be determined, the methodology will require extension, which is part of ongoing studies. When the small strain assumptions are valid, the method outlined in this work is readily

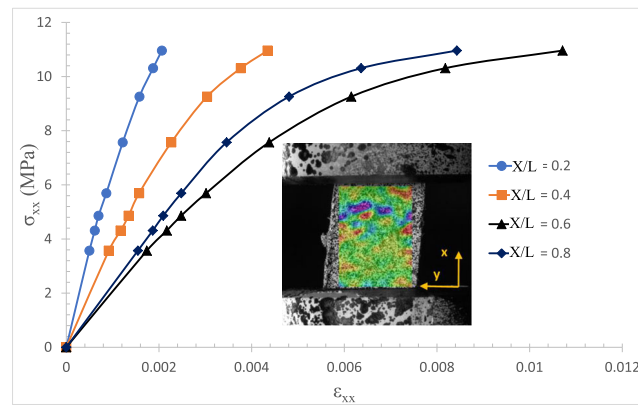


FIGURE 23 Reconstructed $\sigma_{\text{avg}}(x)$ versus $\varepsilon_{\text{avg}}(x)$ response of the bone material at (a) $x = 1.84$ mm, (b) $x = 3.68$ mm, (c) $x = 5.52$ mm and (d) $x = 7.36$ mm along vertical x-axis. $L = 9.18$ mm

extended for non-linear stress strain relationship using the incremental approach, provided that loading is divided into multiple small increments where the strain increments beyond the elastic limit are selected to capture gradients in the stress–strain curve (e.g. at the linear–non-linear transition). For the case of large strain condition, additional steps need to be performed to account for the change in geometry of the sample (area of cross section and node position). These approaches are directly related to the methods implemented in incremental plasticity and updated Lagrangian solutions.

6 | CONCLUSIONS

A direct approach based on finite element principles is demonstrated to obtain the spatial distribution of Young's modulus, $E(x)$, for 1D problems. Results using the 1D material property identification procedure with known spatial distributions of $E(x)$ and axial strain measurements with additive Gaussian noise, β_e , confirm that the methodology converges to the correct $E(x)$ solution for various combinations of experimental data density (N_d) and levels of discretisation (N_e). Application of the method to determine $E(x)$ for a heterogeneous bone sample by using a dense set of experimentally obtained axial strain data using 2D-DIC measurements indicates the predicted distribution is in very good agreement with independently estimated measurements, providing additional confidence in the approach. Finally, using an incremental approach is demonstrated to successfully extend the approach into the non-linear regime and determine the secant modulus distribution, $E_s(x)$, at multiple load levels. The measured $E_s(x)$ is used to determine the local stress–strain response of the heterogeneous bone material at four distinct locations.

ACKNOWLEDGEMENTS

Research was sponsored by the Army Research Laboratory and was accomplished under Cooperative Agreement Number W911NF-20-2-0231. The views and conclusions contained in this document are those of the authors and should not be interpreted as representing the official policies, either expressed or implied, of the Army Research Laboratory or the US government. The US government is authorized to reproduce and distribute reprints for government purposes notwithstanding any copyright notation herein.

CONFLICT OF INTEREST

The authors declare that they have no known competing financial interests or personal relationships that could have appeared to influence the work reported in this paper.

DATA AVAILABILITY STATEMENT

Data available on request from the authors.

SYMBOLS

L	length of specimen (L)
N_e	total number of finite elements for length, L
L_e	L/N_e , the length of each element (L)
$A(x)$	cross-sectional area of specimen at position x (L^2)
M	total number of strain data points along the length, L
N_d	M/N_e , number of strain data points per element
$w(x)$	weighting function in Galerkin finite element formulation
x	spatial position along length of specimen (L)
ξ	local element coordinates (L)
$f(x)$	body force in bar (FL^{-1})
$\sigma(x)$	axial stress in specimen at position x (FL^{-2})
$\epsilon(x)$	axial strain in specimen at position x (L)
δ	applied axial displacement of sample at $x = L$ (L)
P	applied axial load at $x = L$ (F)
σ_{avg}	P/A , average axial stress in the statically loaded specimen (FL^{-2})
$E(x)$	modulus of elasticity at position x (FL^{-2})
E_o	modulus of elasticity at $x = 0$ (FL^{-2})
$\epsilon_N(x)$	$\epsilon(x)/[P/(A E_o)]$ normalised strain at position x
$N(x)$	basis shape functions for each element
J	Jacobian of the transformation between global and local coordinates
E_i	nodal values of $E(x)$ that are defined by the basis shape function, $N(x)$
R_i	right-hand-side vector components
A_{ij}	components of matrix transforming nodal values of $E(x)$, $[A]_{ij} \{E\}_j = \{R\}_i$
β_ϵ	standard deviation of Gaussian strain noise that is added to the exact strain

ORCID

Michael A. Sutton  <https://orcid.org/0000-0002-6946-5047>

REFERENCES

- [1] T. C. Chu, W. F. Ranson, M. A. Sutton, W. H. Peters III, *Exper Mech* **1985**, 25(3), 232.
- [2] P. F. Luo, Y. J. Chao, M. A. Sutton, W. H. Peters, *Exper Mech* **1993**, 33(2), 123.
- [3] H. W. Schreier, J. Braasch, M. A. Sutton, *Opt Eng* **2000**, 39(11), 2915.
- [4] J. D. Helm, M. A. Sutton, S. R. McNeill, *Opt Eng* **2003**, 42(5), 1293.
- [5] J. D. Helm, M. A. Sutton, S. R. McNeill, *Opt Eng* **2003**, 42(5), 1306.
- [6] M. A. Sutton, J. J. Orteu, H. W. Schreier, *Image Correlation for Shape, Motion and Deformation Measurements*. ISBN 978-0-387-78746-6, Springer, New York **2009**.
- [7] K. R. Raghaven, A. E. Yagle, *IEEE Trans. Nucl. Sci.* **1994**, 41(4), 1639.
- [8] F. Kallel, M. Bertrand, *IEEE Trans. Med. Imaging* **1996**, 15(3), 299.
- [9] S. V. Kamat, *Def Sci J* **2009**, 59(6), 605.
- [10] W. Sharpe, Mechanical properties of Mems materials, AFRL-IF-RS-TR-2004-76 Final Technical Report, **2004**. <https://apps.dtic.mil/sti/pdfs/ADA422530.pdf>
- [11] I. Chasiotis, W. Knauss, *Exper Mech* **2002**, 42, 51.
- [12] J. Réthoré, S. Roux, F. Hild, *Eng Fract Mech* **2008**, 75(13), 3763.
- [13] F. Hild, S. Roux, *Strain* **2006**, 42, 69.
- [14] S. Avril, M. Bonnet, A. S. Bretelle, M. Grediac, F. Hild, P. Lenny, F. Latourte, D. Lemosse, S. Pagano, E. Pagnacco, F. Pierron, *Exper Mech* **2008**, 48(4), 381.
- [15] J. Negggers, J. P. M. Hoefnagels, M. G. D. Geers, F. Hild, S. Roux, *Int. J. Numer. Methods Eng.* **2015**, 103(3), 157.
- [16] M. Bertin, F. Hild, S. Roux, F. Mathieu, H. Leclerc, P. Aïmedieu, *J Strain Anal Eng Des* **2016**, 51(2), 118. <https://doi.org/10.1177/0309324715614759>
- [17] J. P. M. Hoefnagels, M. Bertin, C. Du, F. Hild, in *Residual Stress, Thermo-mechanics & Infrared Imaging, Hybrid Techniques and Inverse Problems*, (Eds: A. Baldi, J. Considine, S. Quinn, X. Balandraud) Conference Proceedings of the Society for Experimental Mechanics Series Vol. 8, Springer, Cham **2018**. https://doi.org/10.1007/978-3-319-62899-8_8
- [18] M. I. Friswell, J. E. Mottershead, H. Ahmadian, *Philos. Transact. A Math. Phys. Eng. Sci.* **2001**, 359(1778), 169.

- [19] E. Pagnacco, A. S. Caro-Bretelle, P. Ienny, *Parameter Identification from Mechanical Field Measurements using Finite Element Model Updating Strategies*, ISTE/Wiley, London (UK) **2012**, 247.
- [20] S. Hartmann, R. R. Gilbert, *Comput Mech* **2021**, 68, 633. <https://doi.org/10.1007/s00466-021-01998-3>
- [21] G. Chellini, G. D. Roeck, L. Nardini, W. Salvatore, *J. Constr. Steel Res.* **2010**, 66(3), 398.
- [22] M. A. Sutton, S. R. McNeill, J. D. Helm, Y. J. Chao, *Photomechanics*. Springer Berlin Heidelberg, Berlin, Heidelberg **2000**, 323.
- [23] G. Ellis, in *Control System Design Guide*, Fourth ed. (Ed: G. Ellis), Butterworth-Heinemann, Waltham, MA, USA **2012**, 165.
- [24] S. L. Alexander, C. A. Gunnarsson, K. Rafaels, T. Weerasooriya, *J. Mech. Behav. Biomed. Mater.* **2020**, 102, 103492. <https://doi.org/10.1016/j.jmbbm.2019.103492>
- [25] VIC-2D, Correlated Solutions, Incorporated, 120 Dutchman Blvd, Columbia, SC 29063. www.correlatedsolutions.com
- [26] E. M. C. Jones, M. A. Iadicola, *A Good Practices Guide for Digital Image Correlation*. International Digital Image Correlation Society **2018**. <https://doi.org/10.32720/idics/gpg.ed1>
- [27] V. Gupta, C. Onwuka, A. Kidane, M. A. Sutton, Effect of impact velocity on dynamic response of polymeric foams, Society for Experimental Mechanics – Proposal.

How to cite this article:

S. Rajan-Kattil, M. A. Sutton, S. Sockalingam, F. Thomas, T. Weerasooriya, S. Alexander, *Strain* **2022**, e12427. <https://doi.org/10.1111/str.12427>

APPENDIX A

As noted in Section 3.1, the primary parameters affecting convergence are (a) data density per element, N_d , (b) element size, L_e , and (c) strain error, β_ϵ . Within the matrix $[A]$ defined in Equation (24), the main non-dimensional parameters are $\frac{L}{l_e}(N_e)$, $\Delta\epsilon = \epsilon_0\beta_\epsilon$ and the number of data points in the element (N_d). Based on this observation, the set of non-dimensional parameters used in this work are:

- N_e , number of elements in the discretisation ($N_e = L/l_e$)
- N_d , number of data points within each element ($N_d = M/N_e$, where M is the number of strain data points over the length, L)
- β_ϵ , variability in the strain measurements multiplied by a reference strain, ϵ_0

To determine how N_d affects variability in the predicted modulus for a give number of elements (N_e), additional 1D material property identification procedure were performed for different set of values of N_d and N_e with $\beta_\epsilon = 0.01$. The results are shown in Figure A1. As shown in Figure A1, when N_d is increased for a given N_e , the predicted modulus converges to the exact modulus. Though not shown here, increasing N_e beyond 80 points does not appreciably improve prediction accuracy.

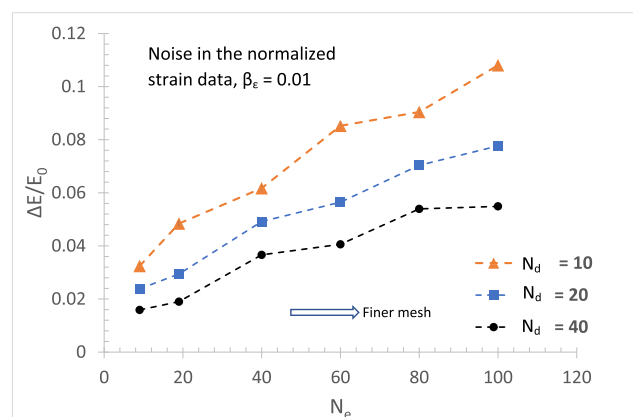


FIGURE A1 $\Delta E/E_0$ versus N_e predictions for $N_d = 10, 20$ and 40 with strain error parameter $\beta_\epsilon = 0.01$ and linearly varying modulus, $E(x)$, defined in Equation (30)

From Figure A1, it can be observed that refinement of the mesh to resolve sharp gradients in the modulus is largely constrained by the spatial resolution of the strain data. For example, if the maximum standard error in the predicted modulus is limited to 5%, an increase in the number of elements from 20 to 40 requires a fourfold increase in data density, which may or may not be achievable with available imaging systems (see additional discussion in Section 3.5.3).

A.1 | Quadratic distribution of Young's modulus with body force component

A problem involving a known body force with a quadratic Young's modulus distribution given by

$$E = E_0 \left(1 + \left(\frac{x}{L} \right)^2 \right) \quad (\text{A1})$$

is analysed here. The body force is taken to be constant along the length and magnitude of the body force is taken to be P/AL . Since the body force term is assumed to be known exactly, the component of the force vector (the right-hand side of Equation (24)) can be readily calculated. Hence, the addition of a body force component has no effect on the predicted modulus.

The exact ε_N strain data obtained using the Young's modulus distribution in Equation (A1) and an applied stress P/A , body force $f(x) = P/AL$ are used to solve Equation (24). For $N_d = 10$, Figure A2a–c presents both Equation (A1) and the predicted distribution of Young's modulus when solving Equation (24) with $L_e = L/4$ (four elements), $L_e = L/8$ and $L_e = L/12$, respectively. Inspection of Figure A2a–c confirms that increasing the number of elements with linear shape functions improves the accuracy of the predictions when noise is absent.

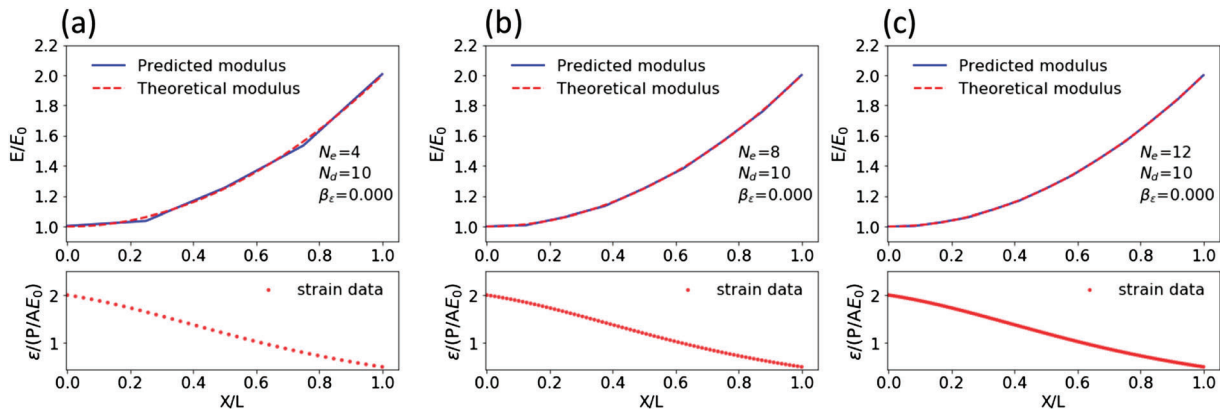


FIGURE A2 Theoretical and predicted $E(x)$ for $N_e = 10$, $\beta_e = 0$ and (a) $L_e = L/4$ (b) $L_e = L/8$ and (c) $L_e = L/12$

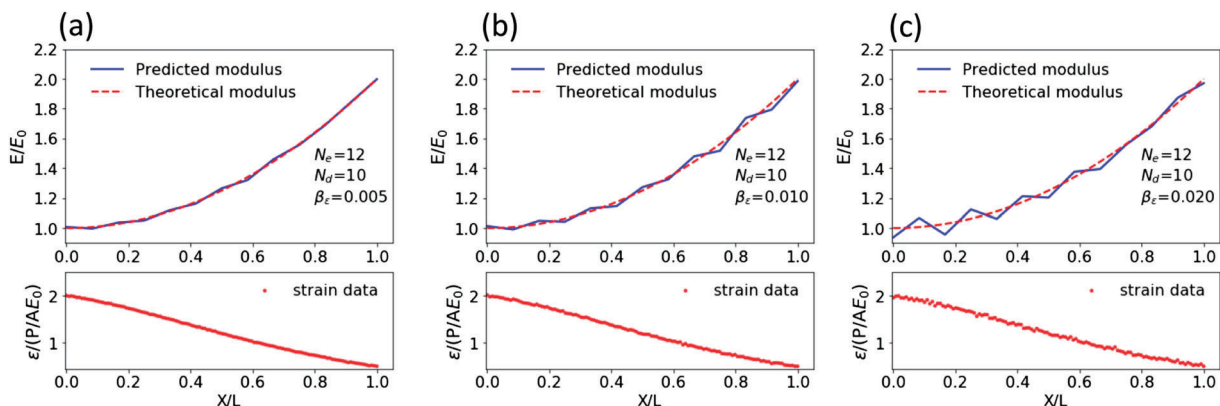


FIGURE A3 Distribution of ε_N and the predicted $E(x)$ for a quadratic modulus distribution with $N_e = 12$, $N_d = 10$ and (a) $\beta_e = 0.005$, (b) $\beta_e = 0.010$ and (c) $\beta_e = 0.020$

To visualise the effect of strain noise on modulus predictions, Figure A3 compares the predicted modulus to the exact modulus distribution when $L_e = L/12$, $N_d = 10$ and (a) $\beta_e = 0.005$, (b) $\beta_e = 0.010$ and (c) $\beta_e = 0.020$. As shown in Figure A3, for a fixed number of strain data per element, as the strain error increases, oscillations in the predicted modulus about the exact solution also increase.

To quantify the effect of N_d on $E(x)$ predictions, for $N_e = 12$ and $\beta_e = 0.020$, Figure A4a–c presents comparisons of the exact quadratic distribution to the predicted $E(x)$ using Equation (24) using $N_d = 20, 80$ and 200 , respectively. Inspection of Figure A4 shows that increasing data density within each element increased the accuracy of the predicted modulus distribution.

Appendix A.2 provides a discussion of the required parameters to obtain a convergent solution for the quadratic distribution in Equation (A1).

A.2 | Convergence parameters for quadratically varying $E(x)$

The effect of parameters N_e , N_d and β_e for a quadratically varying modulus is presented in Figure A5. The dependence of minimum N_d with respect to N_e and β_e are nominally similar to results for linearly varying $E(x)$ shown in Figure 15. However, the minimum data density, N_d , required to obtain convergence for a quadratic variation in $E(x)$ and a fixed combination of N_e and β_e decreases by up to 30% when compared to the results shown in Figure 15. This somewhat

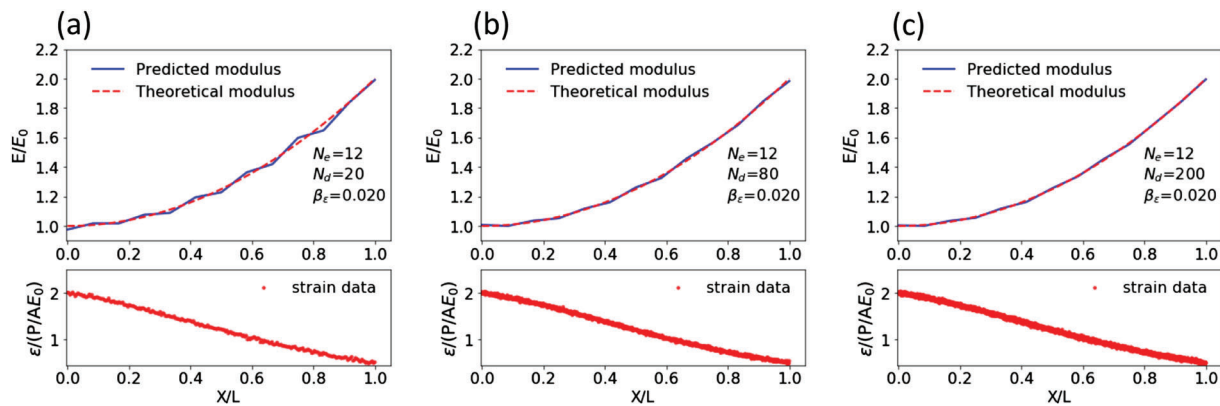


FIGURE A4 Distribution of ϵ_N and the predicted $E(x)$ for a quadratic modulus distribution with $N_e = 12$, $\beta_e = 0.02$ and (a) $N_d = 20$, (b) $N_d = 80$ and (c) $N_d = 200$

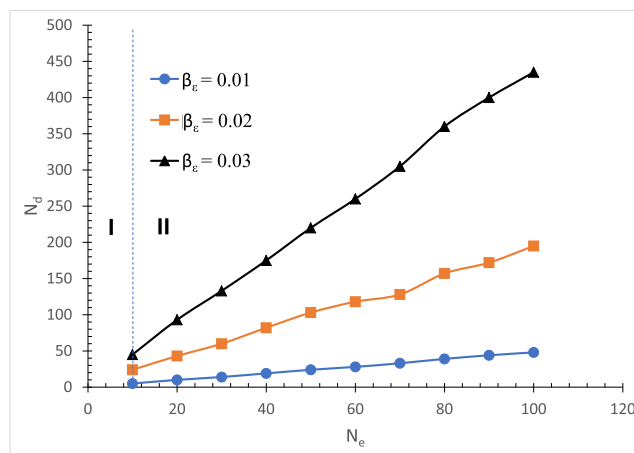


FIGURE A5 Plot of N_d versus N_e for selected values of β_e and quadratic variation in Young's modulus

counter-intuitive result indicates the minimum value of N_d required for convergence depends on the functional form of the modulus variation for a heterogeneous material.

Further inspection of the data in Figure A5 indicates there is a lower bound on the minimum N_e for the quadratically varying modulus, with $N_e \geq 10$ for convergence with $\Delta = 0.04$. For $N_d < 10$, the solution did not converge, independent of N_d . This requirement is directly related to the functional form of $E(x)$.^{##} Hence, the left-side boundary in the parameter space is defined by the minimum value of N_e . In Region I, the effect of the shape of $E(x)$ contributes to defining a lower bound on discretisation that is required for convergence. In Region II, convergence can be obtained with increasing β_e requiring increases in N_d .^{***}

^{##}For the case of the linear shape function used in the current work, it is verified that the FE solutions approaches the true distribution with increasing N_e .

^{***}For the linearly varying $E(x)$ shown in Figure 15, the effect of Zone I is insignificant, and hence is not shown in Figure 15.